MINISTRY OF EDUCATION AND RESEARCH

THE ANNALS OF "DUNAREA DE JOS" UNIVERSITY OF GALATI

Fascicle IX
METALLURGY AND MATERIALS SCIENCE

YEAR XLIII (XLVIII)
June 2025, no. 2

ISSN 2668-4748; e-ISSN 2668-4756

GALATI UNIVERSITY PRESS

2025

EDITORIAL BOARD

THE ANNALS OF "DUNAREA DE JOS" UNIVERSITY OF GALATI
FASCICLE IX. METALLURGY AND MATERIALS SCIENCE
Nº. 2 - 2025, ISSN 2668-4748; e-ISSN 2668-4756
Volume DOI: https://doi.org/10.35219/mms.2025.2

Table of Contents

1. Mihaela MARIN, Florin-Bogdan MARIN - Computer Vision-Based Detection of Patterns in Textile Microscopy Images 5

2. Ionel PETREA, Marian-Iulian NEACSU - Static Analysis of a Converter Vessel Using the Finite Element Method 9

3. Ionuț LAMBRESCU, Mihai Bogdan-ROTH - Assessment Using Numerical Analysis of the Behaviour of a Two Fingers Gripping Mechanism 14

4. Ionuţ LAMBRESCU - On the Optimization of Machined VSD Position for Repaired Pipes 25

5. Andreea ȚÎNTATU - From Mechanical Testing to Decision Making: Selecting a Structural Adhesive Using the Weighted Sum Method 32

6. Beatrice Daniela TUDOR - Studies and Research on Glass Thermoforming 43

7. Mihaela MARIN, Mirela NEGOIAŞ, Florin Bogdan MARIN - Development of a Real-Time Eye Blink Monitoring System Using an IR Sensor and Arduino Microcontroller 49

THE ANNALS OF "DUNAREA DE JOS" UNIVERSITY OF GALATI
FASCICLE IX. METALLURGY AND MATERIALS SCIENCE
Nº. 2 - 2025, ISSN 2668-4748; e-ISSN 2668-4756
Volume DOI: https://doi.org/10.35219/mms.2025.2

THE ANNALS OF "DUNAREA DE JOS" UNIVERSITY OF GALATI
FASCICLE IX. METALLURGY AND MATERIALS SCIENCE
N°. 2 - 2025, ISSN 2668-4748; e-ISSN 2668-4756
Article DOI: https://doi.org/10.35219/mms.2025.2.01

COMPUTER VISION-BASED DETECTION OF PATTERNS IN TEXTILE MICROSCOPY IMAGES

Mihaela MARIN, Florin-Bogdan MARIN
"Dunarea de Jos" University of Galati, Romania
e-mail: florin.marin@ugal.ro

ABSTRACT

The analysis and detection of patterns in textile materials are a critical challenge in modern manufacturing, quality control, and automation processes. Traditional inspection methods, often reliant on manual observation, are not only time-consuming but also prone to inconsistencies. The need for a more precise, efficient, and scalable approach has driven interest in leveraging computer vision for this task. Computer vision systems, powered by advanced algorithms and machine learning models, offer the ability to process and interpret visual data from textile images at high speeds and with greater accuracy.

KEYWORDS: computer vision, textile microscopy images, small batch training

1. Introduction

Computer vision and AI are providing the means of solving defect assessment in an era where automation and intelligent systems are integral to manufacturing processes. In the textile sector, ensuring the quality and consistency of materials is paramount. Traditional manual inspection methods are not only time-consuming but also prone to human error [1, 2]. The microscopic analysis of textile fibres, particularly the detection of patterns, plays a crucial role in assessing material properties such as strength, elasticity, and durability. Moreover, it allows manufacturers to identify errors emerging during the process.

Computer vision, combined with machine learning, offers a promising avenue for automating the analysis of textile microscopy images. By leveraging CNNs, it's possible to extract intricate features from images, facilitating the accurate detection of fiber patterns. However, challenges arise when dealing with limited datasets, necessitating innovative approaches to model training and validation [3, 4].

Fiber patterns in textiles influence the mechanical properties and overall quality of the material. Accurate detection and analysis of these patterns can lead to better control over manufacturing processes and product performance.

Historically, techniques such as optical microscopy and manual counting have been employed to assess fiber patterns. While effective to an extent, these methods lack scalability and are subject to observer variability. Various algorithms have been developed to recognize patterns [5-9].

Recent studies have explored the application of computer vision in textile analysis. For instance, Luo et al. developed a CNN model to distinguish between cashmere and wool fibres, achieving a classification accuracy of approximately 93% [10]. Similarly, FabricNet, an ensemble of CNN architectures, was introduced to recognize various textile fibres, demonstrating the potential of deep learning in this domain [11-13]. In this paper, we propose the integration of ResNet with U-Net to recognize textile patterns using a small batch of training images.

2. Experimental procedure

Given the limited availability of labelled microscopy images, data augmentation becomes essential. Techniques such as rotation, flipping, scaling, and contrast adjustments are employed to artificially expand the dataset, enhancing the model's ability to generalize.

A pre-trained CNN, such as ResNet, was used as the base model. Transfer learning was utilized, where the model's initial layers, trained on a small dataset, are retained, and the final layers are fine-tuned using the textile microscopy images. We used a limited set of our own 70 images for training, representing the patterns of textile to be recognized (Figure 1). The

THE ANNALS OF "DUNAREA DE JOS" UNIVERSITY OF GALATI
FASCICLE IX. METALLURGY AND MATERIALS SCIENCE
Nº. 2 - 2025, ISSN 2668-4748; e-ISSN 2668-4756
Article DOI: https://doi.org/10.35219/mms.2025.2.01

testing set consisted of 40 images (Figure 2). This approach mitigates the challenges posed by limited data.

The model undergoes training with the augmented dataset, employing techniques like early stopping and dropout to prevent overfitting. Validation is conducted using a separate subset of images to assess the model's performance and adjust hyperparameters accordingly.

ResNet introduces residual learning to address the degradation problem in deep networks. By allowing layers to learn residual functions with reference to the layer inputs, ResNet facilitates the training of very deep networks.

Previous studies have applied CNNs to classify textile defects and patterns. For instance, a study utilized a pre-trained ResNet50 model to classify fabric defects into categories like holes and thread errors, achieving notable accuracy.

Transfer learning involves leveraging pre-trained models on large datasets to improve performance on specific tasks with limited data. Fine-tuning adjusts the weights of the pre-trained model to better fit the new task, often leading to improved accuracy.

Fig. 1. *Original textile (no magnification)*

Microscopy images of various textile samples were taken, capturing fine details such as fiber patterns, defects, and texture variations.

Pictures were resized to input sizes expected ResNet models. Rotation, flipping, and contrast variation data augmentation techniques were employed to increase dataset diversity.

ResNet versions (ResNet18, ResNet34, ResNet50) were considered for fine-tuning, based on a balance between model complexity and computational resources. The pre-trained ResNet models were adapted based on the collected dataset. The last fully connected layers were replaced to match the number of classes in the textile dataset. A low learning rate was used to prevent large adjustments to the pre-trained weights. The dataset was divided into a training set and a validation set. The model was trained using cross-entropy loss and optimized using stochastic gradient descent with momentum. Early stopping was implemented to prevent overfitting.

The scarcity of labelled microscopy images poses a significant hurdle. To address this, few-shot learning techniques, such as Siamese Networks, can be implemented. These models are designed to perform well with minimal training examples by learning a similarity function between pairs of inputs.

Differences in microscopy settings can lead to variations in image quality. Standardizing imaging protocols and employing normalization techniques can help reduce this variability.

The batch size determines how many samples are processed before the model parameters are updated, while the learning rate controls the step size for each update. Both hyperparameters need to be carefully tuned to balance training speed and convergence.

To further enhance the model's ability to generalize, data augmentation techniques can be used to artificially expand the training set. For example, random noise can be added to the input features, or the honeycomb geometry can be slightly perturbed. In this research, standard CNNs excel at high-level feature recognition but struggle with spatial resolution, especially when detecting small or fine-grained patterns. In textile microscopy, features such as fiber patterns or micro-defects may be minute and easily lost in deep network architectures. U-Net, a popular architecture for biomedical image segmentation, excels at combining low-level spatial details with high-level semantic features, but it can benefit from stronger feature extractors. A pre-trained ResNet-50 model (without the final classification head) is used as the encoder in the U-Net. The residual blocks provide robust multi-scale feature extraction, which is crucial for recognizing fine textile features. The decoder reconstructs the image from the low-resolution feature maps, using up-convolutions (transpose convolutions) and skip connections from the encoder layers to retain spatial detail.

Skip connections bridge the encoder and decoder at multiple levels, allowing fine details from early layers to influence the final segmentation. Transfer learning, by means of the ResNet encoder, is initialized with weights pre-trained on ImageNet, providing a strong starting point for feature extraction.

We developed the application in Visual Studio Code, and the model was trained in Pytorch.

3. Results and discussions

The fine-tuned ResNet models achieved high accuracy in classifying small features in textile

THE ANNALS OF "DUNAREA DE JOS" UNIVERSITY OF GALATI
FASCICLE IX. METALLURGY AND MATERIALS SCIENCE
Nº. 2 - 2025, ISSN 2668-4748; e-ISSN 2668-4756
Article DOI: https://doi.org/10.35219/mms.2025.2.01

microscopy images. The Dice Score and Intersection over Union (IoU) are both metrics used to evaluate the accuracy of image segmentation models (e.g., models that identify objects in an image, like segmenting an object from the background).

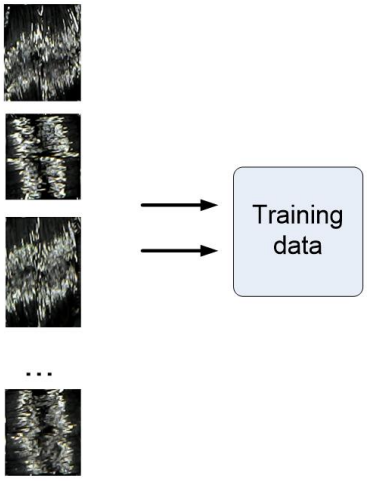

Fig. 2. *Training data consisting of small batch of images*

Intersection over Union (IoU) measures the overlap between the predicted mask and the ground truth mask (Figure 2). The formula is:

$$IoU = \frac{Area\ of\ Overlap}{Area\ of\ Union} = \frac{TP}{TP + FP + FN}$$

where TP = True Positives (correctly predicted pixels); FP = False Positives (incorrectly predicted as part of object); and FN = False Negatives (missed pixels).

Table 1 depicts the results, showing that integrating ResNet and U-net provides and improved solution for the specific task of identifying textile patterns, compared to using only U-Net.

Experiments were conducted on the textile microscopy dataset, with evaluation metrics including Dice score, Intersection over Union (IoU), precision, and recall (Figure 3).

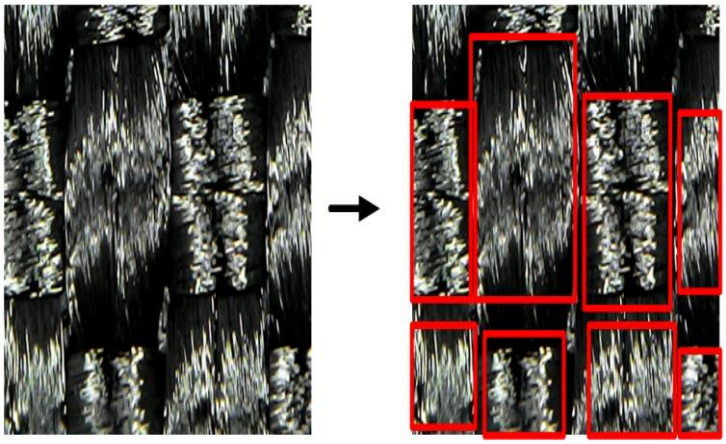

Fig. 3. *Recognition of textile paterns*

Tabel 1. *Results of the developed algorithm*

Model	Dice Score	IoU Score	Precision	Recall
U-Net (baseline)	0.74	0.62	0.8	0.73
ResNet-U-Net	**0.83**	**0.73**	**0.87**	**0.83**

4. Conclusions

The integration of ResNet with U-Net offers a powerful architecture for textile microscopy image segmentation, enabling accurate recognition of small, intricate features such as fiber patterns and defects. This approach addresses the limitations of standard CNN classifiers and U-Net models when used independently. By leveraging transfer learning and a robust encoder-decoder structure, the ResNet-U-Net hybrid demonstrates strong potential for practical applications in textile quality control and research.

Future work might include exploring self-supervised pretraining on unlabelled microscopy data and optimizing models for real-time analysis in textile manufacturing.

References

[1]. Hanbay K., Talu M. F., Özgüven Ö. F., *Fabric defect detection systems and methods - A systematic literature review*, Optik, vol. 127, p. 11960-11973, 2016.
[2]. Kumar A., *Computer-Vision-Based Fabric Defect Detection: A Survey*, IEEE Transactions on Industrial Electronics, vol. 55, no. 1, p. 348-363, Jan. 2008.
[3]. Abdel-Azim G., Nasri S., *Textile defects identification based on neural networks and mutual information,* International Conference on Computer Applications Technology (ICCAT), 2013.
[4]. Sujee R., Padmavathi S., *Image enhancement through pyramid histogram matching*, International Conference on Computer Communication and Informatics (ICCCI), 2017.
[5]. Rebhi A., Abid S., Fnaiech F., *Fabric defect detection using local homogeneity and morphological image processing*, International Image Processing, Applications and Systems (IPAS), Hammamet, 2016.
[6]. Jmali M., Zitouni B., Sakli F., *Fabrics defects detecting using image processing and neural networks*, Information and Communication Technologies Innovation and Application, 2014.
[7]. Jeong H., Park K., Ha Y., *Image Preprocessing for Efficient Training of YOLO Deep Learning Networks*, IEEE International Conference on Big Data and Smart Computing (BigComp), Shanghai, 2018.
[8]. Latif A. Rasheed, Sajid U., *et al.*, *Content-based image retrieval and feature extraction: a comprehensive review*, Mathematical Problems in Engineering, vol. 2019, Article ID 9658350, 2019.
[8]. Kumar A., *Computer-vision-based fabric defect detection: a survey*, IEEE Transactions on Industrial Electronics, vol. 55, no. 1, p. 348-363, 2008.
[9]. Boshan Shi, *et al.*, *Fabric defect detection via lowrank decomposition with gradient information and structured graph algorithm*, Information Sciences, vol. 546, 2021.
[10]. Junli Luo, *et al.*, *Cashmere and wool identification based on convolutional neural network*, Sage, 2023.
[11] Ngai W. T., *et al.*, *Decision support and intelligent systems in the textile and apparel supply chain: an academic review of research articles*, Expert Systems with Applications, vol. 41, no. 1, p. 81-91, 2014.
[12]. Guohua Liu, Xiangtong Zheng, *Fabric defect detection based on information entropy and frequency domain saliency*, The Visual Computer, vol. 37, 2020.
[13]. Hong-wei Zhang, *et al.*, *Yarn-dyed Fabric Defect Detection using U- shaped De-noising Convolutional Auto-Encoder*, IEEE 9th Data Driven Control and Learning S Reystems Conference (DDCLS), Liuzhou, China, 2020.

THE ANNALS OF "DUNAREA DE JOS" UNIVERSITY OF GALATI
FASCICLE IX. METALLURGY AND MATERIALS SCIENCE
No. 2 - 2025, ISSN 2668-4748; e-ISSN 2668-4756
Article DOI: https://doi.org/10.35219/mms.2025.2.02

STATIC ANALYSIS OF A CONVERTER VESSEL USING THE FINITE ELEMENT METHOD

Ionel PETREA, Marian-Iulian NEACSU
"Dunarea de Jos" University of Galati, Romania
e-mail: ionel.petrea@ugal.ro, mneacsu@ugal.ro

ABSTRACT

The paper presents static and fatigue strength calculations for a converter. Following common practice with liquid steel vessels, the calculations were evaluated in accordance with the 2007 edition of the ASME Boiler and Pressure Vessel Code, Section VIII.

KEYWORDS: finite element, mechanical structures, converter, mechanical stresses

1. General description of the calculation method

For all calculations, a finite element model of the converter system was generated [1-3]. The calculations focused on the removable part of the vessel (in particular, the suspension system). Therefore, only the vertical position of the converter (0° - Blowing) was analysed [3, 4].

The results of the static analysis were evaluated according to the ASME Boiler and Pressure Vessel Code. The stress evaluation showed that the vessel shell (i.e. the flange connection of the removable part) is adequately designed for the investigated loads in terms of static stresses and fatigue. Therefore, a fundamental prerequisite is that the requirements described below are fully met [5-7].

As with any welded structure, common maintenance practice requires regular inspection of the welded connections for crack initiation (VT and PT and/or MT/UT), typically performed every 1-2 years.

The following requirements can be deduced from the calculation results [8]:

- In the structural areas of the vessel shell with higher loads - i.e., the welds between the ribs and the flange of the upper part of the vessel - full penetration welds must be made, and these must be 100% non-destructively tested (VT, PT/MT, and UT/RT);
- Areas with higher loads must be inspected regularly;
- The calculation of the bolts and shafts must be carried out by a competent entity;
- The prestressing of the bolts was not taken into account in the FEM calculation.

In the calculation model, linear elastic stress-strain behaviour was assumed for all components. The corresponding material properties were based on data for comparable materials according to the SEW standard (Physical Properties of Steels) and were adjusted to reflect the temperatures of the components.

The material properties used are as follows:

- Vessel Shell (material: 16Mo3 / 400 °C);
- Young's modulus of elasticity E = 184 GPa;
- Poisson's ratio of elasticity; v = 0.3.

The maximum temperature of the vessel shell was specified as 400 °C. No equilibrium temperature calculation was performed.

2. Finite element analysis (FEM)

The computational model comprises the vessel, the converter ring, the ring shafts, the four lamellar suspension systems and the horizontal suspension (Figure 1). Due to the symmetrical design, only half of the model was used. The mass of the complete steel structure of the converter assembly, including the refractory, is 268 tonnes. The complete converter ring weighs 109 tonnes and the suspension system was assumed to weigh 9 tonnes. Thus, the total mass of the model (including deposits) amounts to 193 tonnes for the half-model.

THE ANNALS OF "DUNAREA DE JOS" UNIVERSITY OF GALATI
FASCICLE IX. METALLURGY AND MATERIALS SCIENCE
No. 2 - 2025, ISSN 2668-4748; e-ISSN 2668-4756
Article DOI: https://doi.org/10.35219/mms.2025.2.02

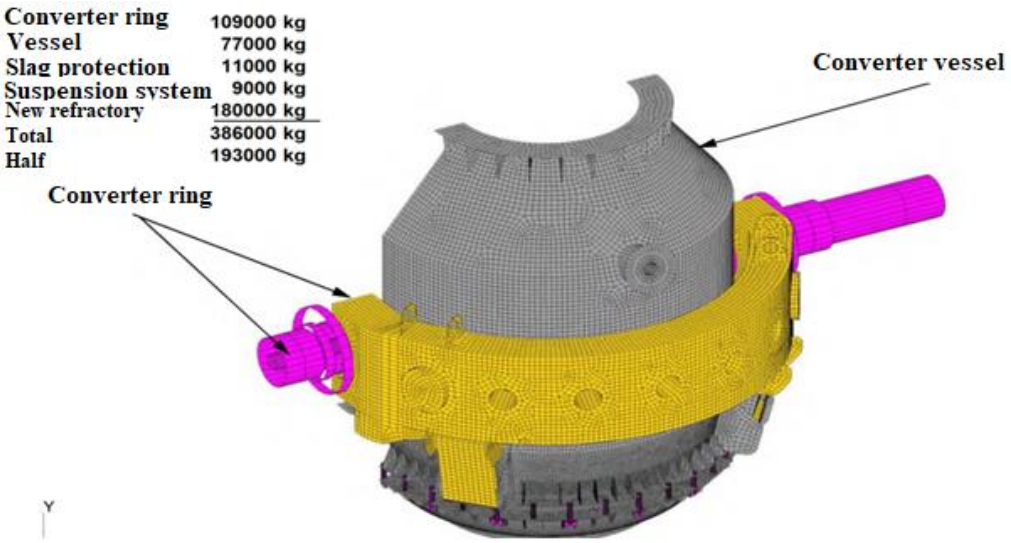

Fig. 1. *Calculation model*

2.1. Model discretization

The mesh was constructed with four linear nodes in the form of quadrilaterals for the vessel shell elements, using a bilinear extrapolation of the corner stresses.

As can be seen from Figure 2, the computational model was generated with a relatively high mesh density, which allows a good degree of discretization and, therefore, produces quite accurate stress results.

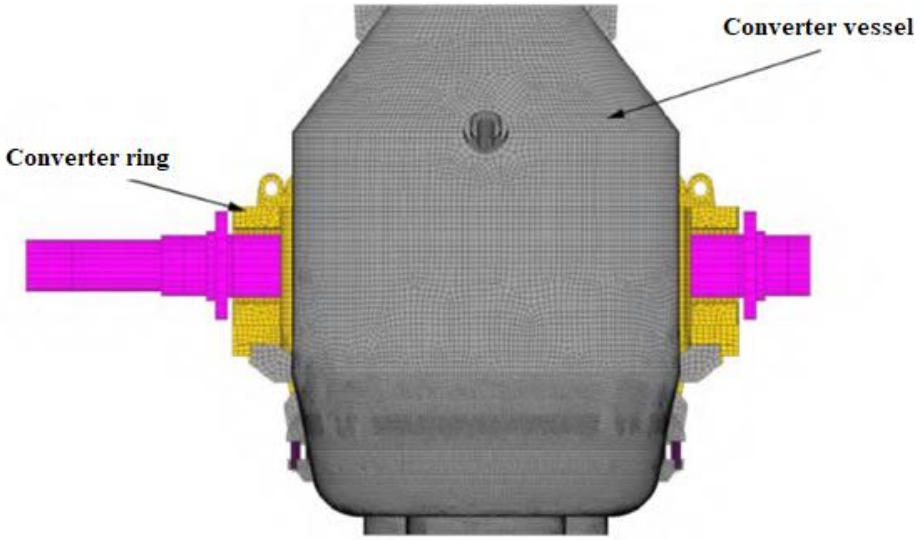

Fig. 2. *The network of nodes and elements – mesh*

2.2. Applying restrictions and constraints – Figure 3 [8]

The entire model is fixed to the converter ring shafts. In addition, the boundary conditions were applied symmetrically in the section plane.

2.3. Specification of the demands

The loads considered for the blowing are represented in Figure 4. In addition to the static load of 1893 kN for half of the converter, the liquid content of 387 kN (liquid steel, slag, and deposits) was considered as ferrostatic pressure.

THE ANNALS OF "DUNAREA DE JOS" UNIVERSITY OF GALATI
FASCICLE IX. METALLURGY AND MATERIALS SCIENCE
No. 2 - 2025, ISSN 2668-4748; e-ISSN 2668-4756
Article DOI: https://doi.org/10.35219/mms.2025.2.02

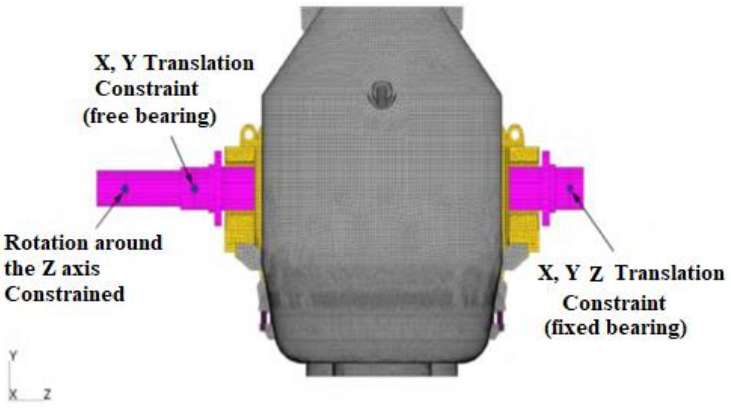

Fig. 3. *Restrictions and constraints*

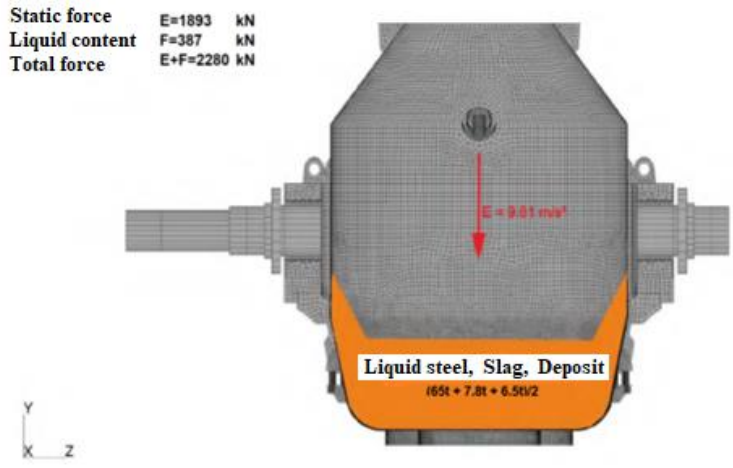

Fig. 4. *Requests*

3. Results obtained

3.1. Static resistance assessment

The main results of the finite element calculations are the displacements and stresses. Representative displacements understatic loads are shown in Figure 5. A maximum vertical displacement of 3.07 mm was calculated. The maximum distance between the two parts of the vessel amounts to 0.13 mm without tightening. This gap must be overcome by adequate tightening of the bolts.

The static stresses are represented in Figures 6 and 7. As already mentioned, the assessment focuses mainly on the suspension system of the lower part of the vessel.

The stresses in this area are shown in detail in Figure 7. The maximum stress in this region amounts to 104 MPa at the edge of the cutout of a suspension bolt. This value is safely below the limit of 127 MPa (valid for 400 °C). Therefore, it can be stated that the suspension of the lower part of the vessel is sufficiently designed with respect to the primary and secondary (static) stresses.

Fig. 5. *Displacements*

THE ANNALS OF "DUNAREA DE JOS" UNIVERSITY OF GALATI
FASCICLE IX. METALLURGY AND MATERIALS SCIENCE
No. 2 - 2025, ISSN 2668-4748; e-ISSN 2668-4756
Article DOI: https://doi.org/10.35219/mms.2025.2.02

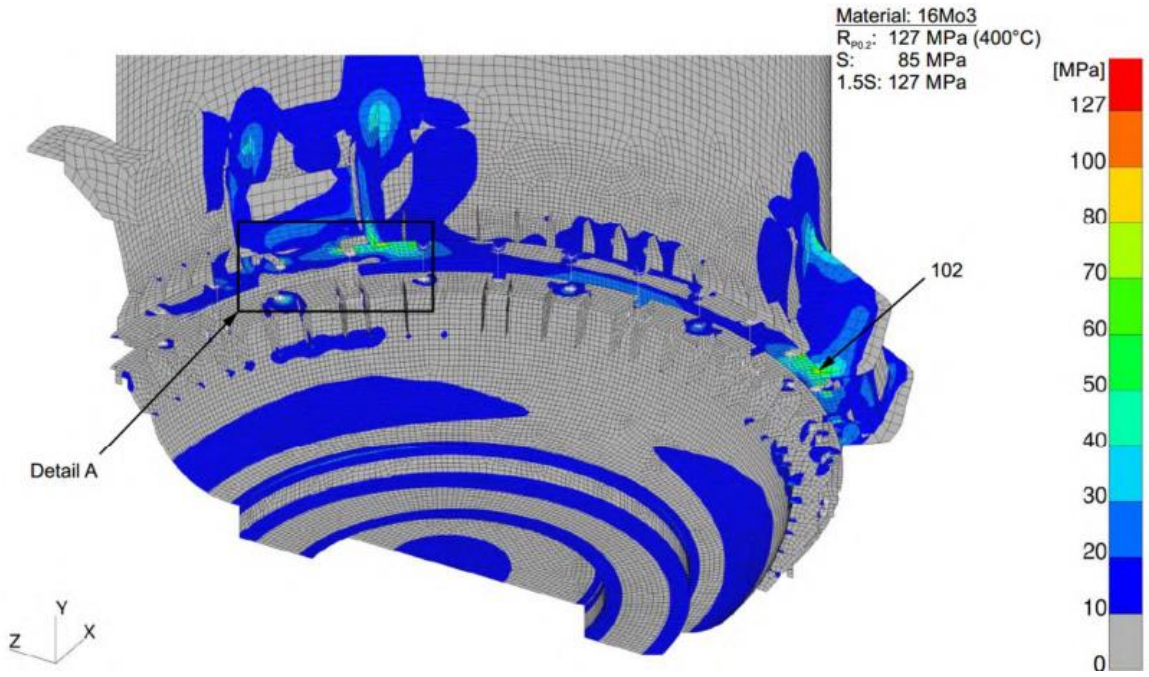

Fig. 6. *The von Mises stress field*

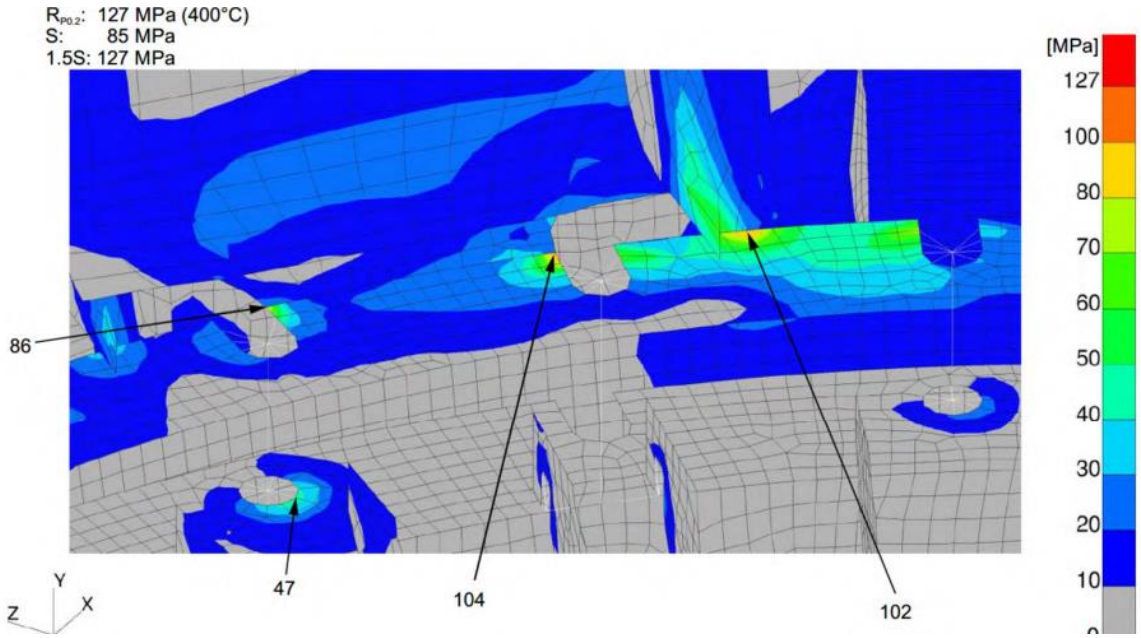

Fig. 7. *Stress field – detail A*

3.2. Fatigue resistance assessment

For the 65-ton capacity converter, normal operation with new refractory insulation was evaluated. Furthermore, a total number of operating cycles for the converter system of N = 210000 was specified. This number of cycles corresponds to 30 loads per day, 350 days per year, and 20 years of life. The number of equivalent load cycles for the vertical suspension amounts to 312000. This number was calculated using the operating scheme of a similar converter.

The permissible stress range, in terms of fatigue for different types of welds and for the actual number of load cycles, is given by the following values:

- Permissible stress amplitude for the unwelded material and for a fully penetrated machined weld: 105 MPa.

THE ANNALS OF "DUNAREA DE JOS" UNIVERSITY OF GALATI
FASCICLE IX. METALLURGY AND MATERIALS SCIENCE
No. 2 - 2025, ISSN 2668-4748; e-ISSN 2668-4756
Article DOI: https://doi.org/10.35219/mms.2025.2.02

- Allowable stress amplitude for a full penetration weld: 88 MPa.

The static stresses for the 0° - Blow position were assumed to be the stress amplitude, which results in a larger stress range than in reality. The total maximum of 104 MPa is below the limit Sa=105 MPa. The maximum stress in the welded areas amounts to 76 MPa, which is below the limit of 88 MPa (full penetration weld). Therefore, these ribs must be welded with a full penetration weld on the flange. No machining is required.

4. Conclusions

To sum up, it can be stated that the investigated components of the converter system meet the requirements of the applicable standards (ASME Standard) under the considered operating load conditions.

Therefore, the fundamental conditions are that the strength properties of the applied components reach at least the evaluated data and that the manufacture of the converter components is carried out in strict accordance with the design drawings.

References

[1]. Marin C., *et al.*, *Modelarea cu elemente finite a structurilor mecanice-2002*, Editura Academiei Române şi Editura AGIR, ISBN 973-27-0957-X and ISBN 973-8130-98-0.
[2]. Mănescu T. Ş., *Analiză structurală prin metoda elementului finit*, Timişoara: Orizonturi Universitare, ISBN 973-638-217-6, 2005.
[3]. Comsa D. S., *Metoda elementelor finite*, Editura U.T. PRES-Cluj-Napoca, 2007.
[4]. Sohoran Ş., Petre C. C., *Programe şi aplicaţii cu elemente finite*, Editura Printech, ISBN: 973-718-005-4, Sept. 2007.
[5]. Pantel E., Bia C., *Metoda elementelor finite pentru structuri de rezistenta*, Editura Todesco, 2009.
[6]. Ghionea I. G., *Proiectare asistată în CATIA V5*, Editura Bren, Bucureşti, 2007.
[7]. Mogan GH. L., Butnariu S. L., *Analiza cu elemente finite in inginerie, Aplicatii practice in CATIA*, Editura Universitetii Transilvania din Brasov, 2007.
[8]. Lambrescu I., Diniță A., *Analiza structurilor ingineresti prin utilizarea metodei elementului finit*, Aplicatii in ANSYS, Editura Matrixrom, București, 2011.

THE ANNALS OF "DUNAREA DE JOS" UNIVERSITY OF GALATI
FASCICLE IX. METALLURGY AND MATERIALS SCIENCE
No. 2 - 2025, ISSN 2668-4748; e-ISSN 2668-4756
Article DOI: https://doi.org/10.35219/mms.2025.2.03

ASSESSMENT USING NUMERICAL ANALYSIS OF THE BEHAVIOUR OF A TWO FINGERS GRIPPING MECHANISM

Ionuț LAMBRESCU, Mihai Bogdan-ROTH
Universitatea Petrol-Gaze din Ploiești, Bd. București 39, Ploiești, Romania
e-mail: ilambrescu@upg-ploiești.ro

ABSTRACT

An important issue in robotics is evaluating the force necessary to firmly grip objects. This can be done experimentally, or, as a more cost-effective approach, through numerical analysis. The results obtained through this method, although less precise, can offer a good assessment of the way a gripping mechanism behaves. The authors propose a comparative numerical analysis of a two-finger gripper, using a motion analysis performed in Siemens NX and a transient structural analysis conducted in Ansys. Both methods aim to capture the moment when the grasped object starts to slip. This moment marks the point at which the gripping is no longer reliable and provides insights into the reliability of the gripping mechanism. To assess the influence of the geometry of the gripping area, as well as the impact of the shape of the grasped object or the pair of materials (object and gripper), several analyses were performed in both Siemens NX and Ansys Workbench.

KEYWORDS: Gripping mechanisms, Grippers, Finite element, Motion analysis

1. Introduction

The problem of calculating/evaluating the force necessary for a firm grasp is of paramount importance in robotics. The literature covers this topic for a wide variety of grippers, in terms of their shape, number, material, etc. Some researchers analysed a static problem, while others considered the situation when the gripped object is moving (with a certain velocity or acceleration) [1, 2]. The proposed approaches were analytical, experimental, or numerical (or a combination of them). From the point of view of the shape of the grasped object, irregularly shaped objects are encountered in many cases [3-8].

The authors of this paper focused their research in two directions:

- To evaluate the friction coefficient for three pairs of materials: aluminium-aluminium, aluminium - Necuron and Necuron-Necuron;
- To include the determined friction coefficient in the analysis of a two-finger gripper (with different geometries in the grasping region – see Figure 1) used for grasping bodies of parallelepipedal, cylindrical, hyperboloidal, and barrel-like shapes (see Figure 2).

The analyses performed were done using (for comparison and validation) a motion analysis conducted in Siemens NX and a transient structural analysis carried out in Ansys Workbench. The main purpose of the analysis was to evaluate the influence of the grasped object shape and the geometry of the fingers' grasping area on the force necessary to retain the grasped object. Like other researchers [2, 9], we were interested in capturing the moment when the grasped object starts to slip. These moments in time, for various shapes of the grasped object and geometries of the fingers' contact areas, were compared to detect the influence they have on the stability of the grip.

The results will be presented in graphical format to allow the assessment of the influence that the object shape and the finger grasping region geometry have on the moment of inception of the slipping process.

THE ANNALS OF "DUNAREA DE JOS" UNIVERSITY OF GALATI
FASCICLE IX. METALLURGY AND MATERIALS SCIENCE
Nº. 2 - 2025, ISSN 2668-4748; e-ISSN 2668-4756
Article DOI: https://doi.org/10.35219/mms.2025.2.03

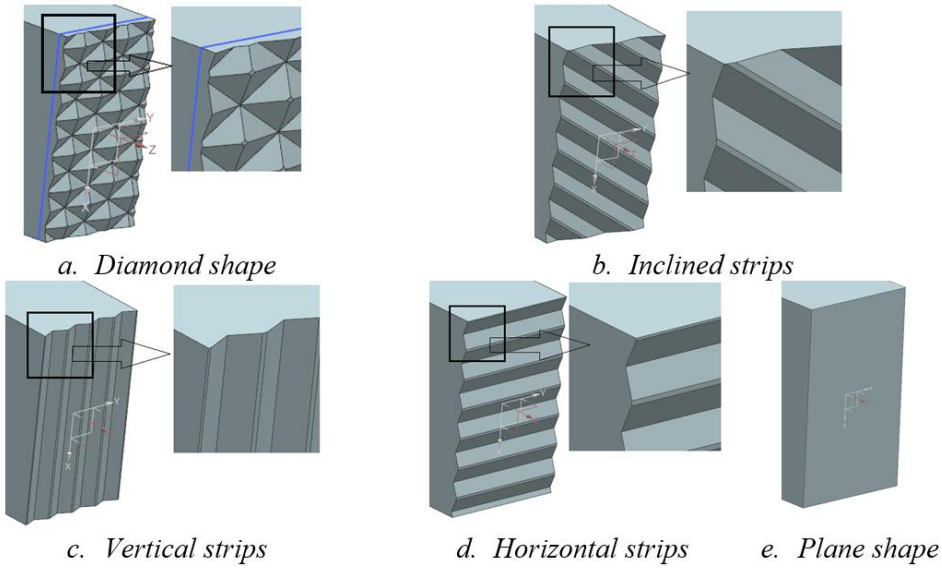

Fig. 1. *Geometries of the grasping region*

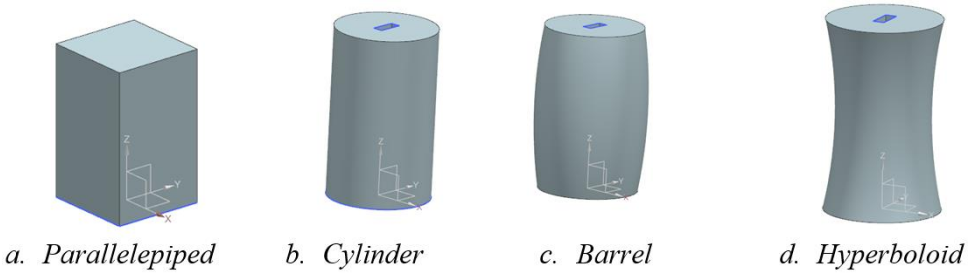

Fig. 2. *Shapes of the grasped objects*

2. Method

The workflow the authors propose is the following:

- Experimental determination of the friction coefficient for three material pairs: aluminum-aluminum, aluminum – Necuron (Necuron is a polymeric material with good performance in bending, compression and abrasion. It is used for tools, sheet metal forming, moulds for plastic deformation of metals, and prototypes for copying, etc. It can be glued with K8 and K13 adhesives. All the above-mentioned properties make Necuron a material worth considering for applications in robotics), and Necuron-Necuron;
- Capturing the moment of inception of slipping of the grasped object using a motion simulation in Siemens NX;
- Capturing the moment of inception of slipping of the grasped object using a transient structural analysis in Ansys Workbench (for the aluminum – aluminum pair only);
- Comparing and interpretation of the results.

Figure 3 provides details on the model used in the numerical analysis (motion simulation in Siemens NX).

The two fingers are pushed towards the object (they are in contact from the beginning) with forces acting along the two arrows, and with intensity described by the plot: the force remains constant for 0.2 seconds, then decays to zero over the next 0.8 seconds. The object rests on a moving base that executes a translation, as indicated by the arrow, at a speed of 200 mm/sec. After 0.2 seconds, the object is no longer supported by the moving base. As long as the two normal forces are sufficiently large, the object remains stationary. It will begin to slip when the normal forces no longer provide a frictional force capable of supporting the object's weight. This critical moment will be identified through numerical analysis.

THE ANNALS OF "DUNAREA DE JOS" UNIVERSITY OF GALATI
FASCICLE IX. METALLURGY AND MATERIALS SCIENCE
No. 2 - 2025, ISSN 2668-4748; e-ISSN 2668-4756
Article DOI: https://doi.org/10.35219/mms.2025.2.03

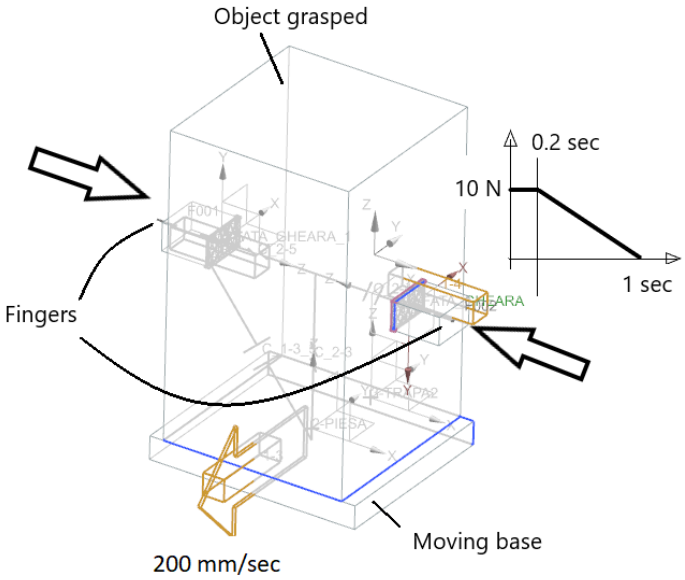

Fig. 3. *The model for the analysis*

3. Determination of the friction coefficient

There are different methods presented in the literature for the experimental determination of the friction coefficient. We refer here to the contributions of [10-13]. The authors designed and built an original device for determining the friction coefficient for different pairs of materials – see Figure 4.

Basically, a normal force is applied to parts 1 and 2, which are in contact with the weighted object (part 5). The friction force holds this object in place if the normal forces have the required value. The applied force is continuously measured using the precision scale (part 3). The value of the normal force is controlled by the adjustment screw (part 4). When the normal force falls below a certain threshold, object 5 starts to slip.

Each determination is filmed. After each test, the AVI file is analysed using software that detects the moment the object begins to slip (move), and the corresponding normal force value is read from the display of the precision scale. Since the weight of object 5 and the normal force are known, it is straightforward to calculate the friction coefficient.

To assure reliable results, 201 determinations were carried out and statistically processed. After performing the Kolmogorov-Smirnov and the Shapiro-Wilk tests [14], which confirmed the normal distribution of the data, a mean value for the friction coefficient was calculated – see Figures 5a and 5b. After a simple calculation, the resulting friction coefficients for the three analysed material pairs were:

- aluminium-aluminium: 0.305;
- aluminium-Necuron: 0.318;
- Necuron-Necuron: 0.39.

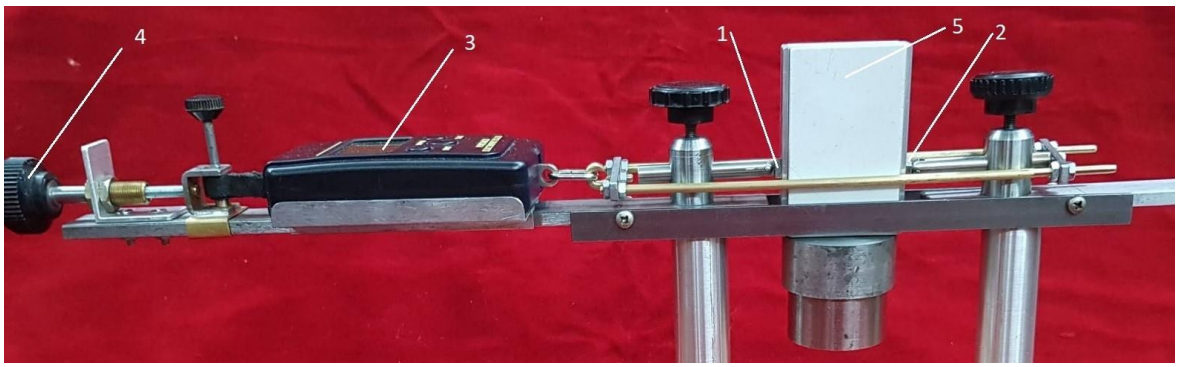

Fig. 4. *Device for measuring the friction coefficient*

THE ANNALS OF "DUNAREA DE JOS" UNIVERSITY OF GALATI
FASCICLE IX. METALLURGY AND MATERIALS SCIENCE
Nº. 2 - 2025, ISSN 2668-4748; e-ISSN 2668-4756
Article DOI: https://doi.org/10.35219/mms.2025.2.03

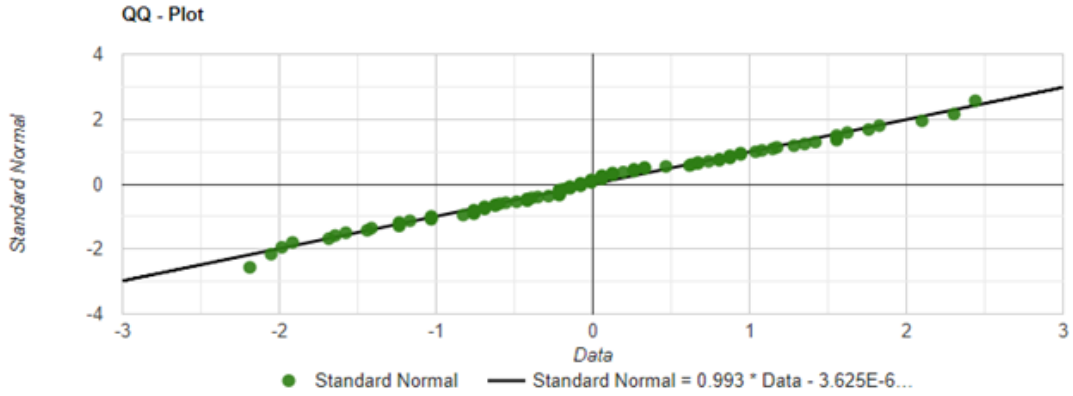

a) Standard Normal Distribution

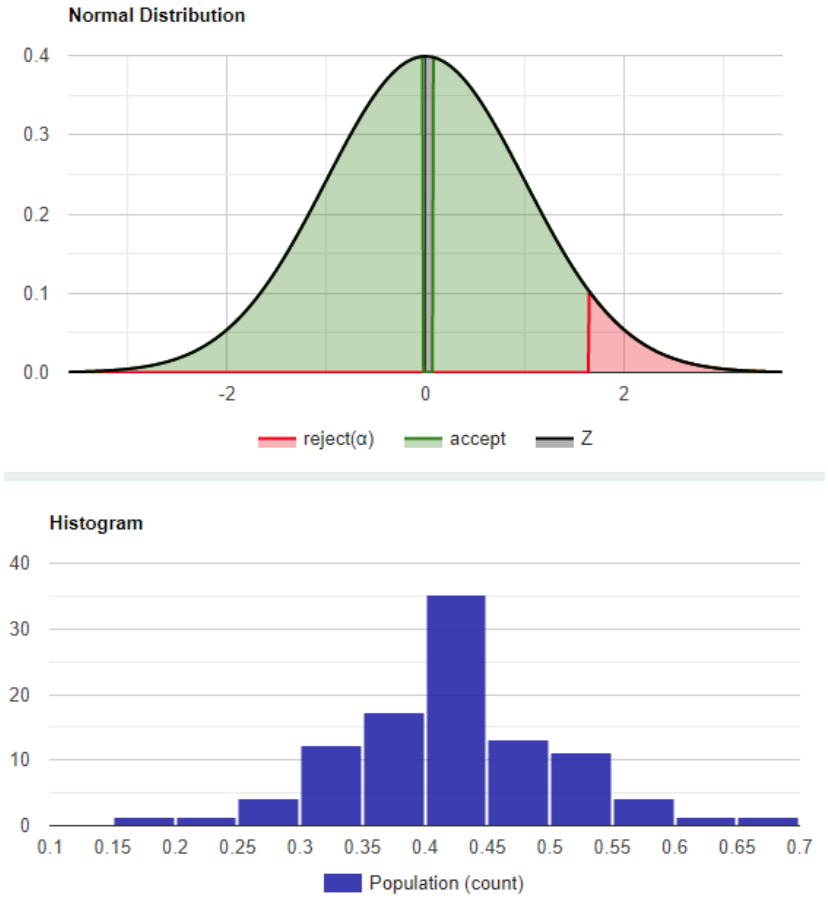

b) Normal distribution

Fig. 5. *Results of the Shapiro-Wilk test*

4. Dynamic analysis in Siemens NX

Figure 6 presents the model used in the Siemens NX dynamic simulation [15, 16]. Frame 1 is fixed. The Motion Base (part 3), as explained in the Method section and shown in Figure 3, moves and, after 0.2 seconds, leaves Object 2 with no support other than the friction forces acting between Object 2 and Fingers 4 and 5. When the normal forces applied through Fingers 4 and 5 on Object 2 become sufficiently small, Object 2 will begin to slip. Joints and 3D contacts were also defined in the simulation, and their names in the simulation tree indicate the bodies they connect - see Figure 6. The simulation was run for a duration of 1 second, with 200 equally spaced time steps.

THE ANNALS OF "DUNAREA DE JOS" UNIVERSITY OF GALATI
FASCICLE IX. METALLURGY AND MATERIALS SCIENCE
No. 2 - 2025, ISSN 2668-4748; e-ISSN 2668-4756
Article DOI: https://doi.org/10.35219/mms.2025.2.03

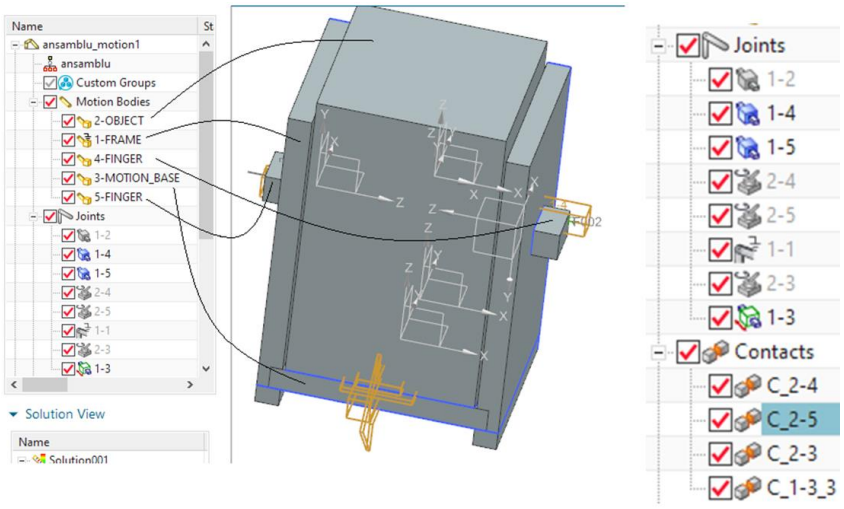

Fig. 6. *Model for the Siemens NX dynamic simulation*

After the analyses were performed for the different object shapes and finger geometries, results such as displacements, velocities, accelerations, and forces were obtained. These will be presented and discussed in Results and Conclusions sections.

5. Transient structural analysis in Ansys Workbench

Figure 7 presents the model used in the Ansys Workbench transient structural analysis [17]. The model is simpler than that used in the dynamic analysis performed in Siemens NX Motion. It includes one half of the Object and a Finger, with symmetry applied. This approach ensures a significant reduction in the number of elements.

Frictional contact has been defined between the half-Object and the Finger. Surface guides have also been defined for both components to ensure accurate replication of real-world boundary conditions. A force with a variation similar to that used in the Siemens NX motion analysis is applied to the Finger to produce friction between the Object and the Finger. After the analysis, results including displacements, velocities, accelerations, stress distributions, and contact conditions were obtained. These will be presented and discussed in Results and Conclusions sections.

The main settings of the transient structural analysis are as follows:

- Minimum time step: 0.001 seconds;
- Moderate speed dynamic;
- Large deflections: ON.

The minimum element size in the finger grasping area is 0.125 mm.

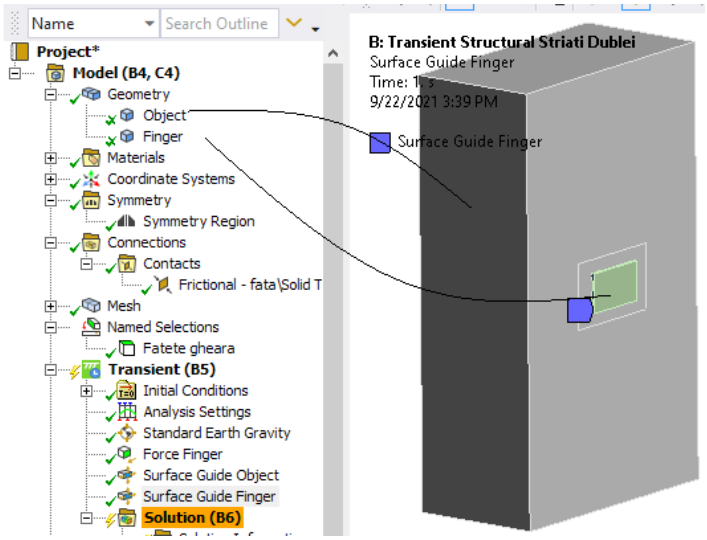

Fig. 7. *Model for the Ansys Workbench transient structural simulation*

THE ANNALS OF "DUNAREA DE JOS" UNIVERSITY OF GALATI
FASCICLE IX. METALLURGY AND MATERIALS SCIENCE
No. 2 - 2025, ISSN 2668-4748; e-ISSN 2668-4756
Article DOI: https://doi.org/10.35219/mms.2025.2.03

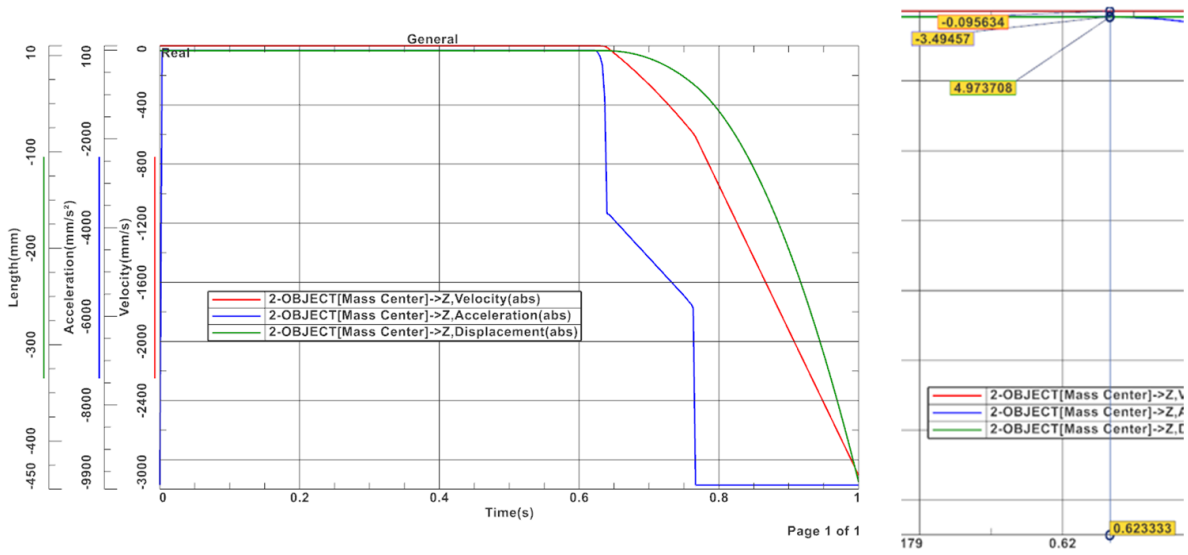

a) Overall view *b) Detail view*

Fig. 8. *Displacement [mm], velocity [mm/sec], acceleration [mm/sec^2] in the vertical direction*

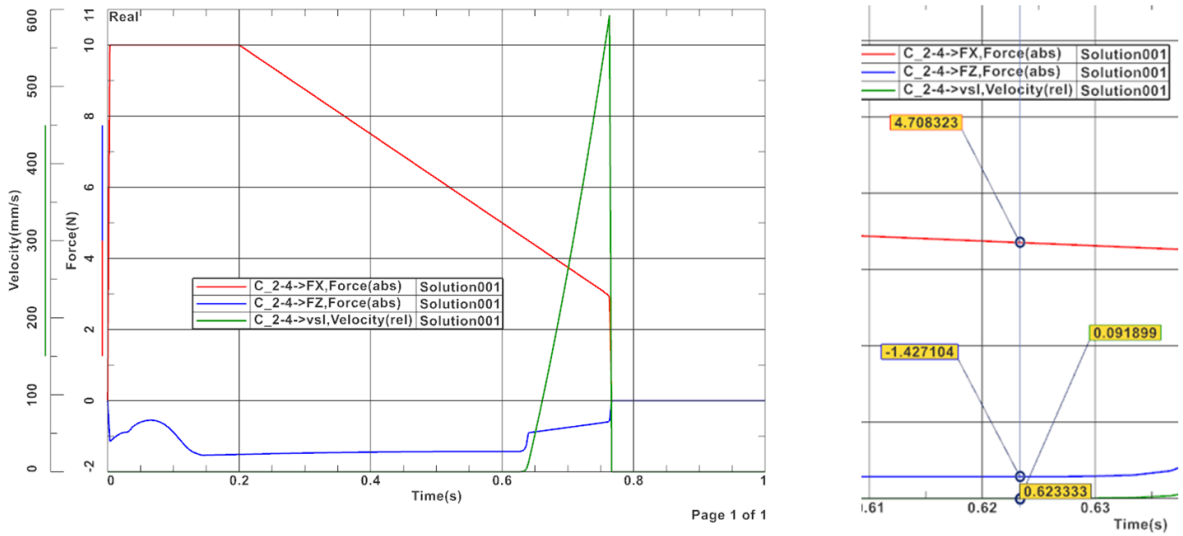

a) Overall view *b) Detail view*

Fig. 9. *Normal force (Fx), Friction force (Fz) [N] and Sliding velocity [mm/sec^2]*

As in the case of the motion analysis, using these plots and the accompanying tables, we can detect the moment when the object begins to slip. In the case of the data presented in Figures 10 and 11, we can observe that slipping starts at 0.625 seconds, which is very close to the moment detected in the Siemens NX motion analysis (0.623 seconds).

In the following plots, we will present the results obtained for all object shapes, finger geometries (in the grasping area), and material pairs, based on the motion analysis performed in Siemens NX. It is important to note that, regardless of the Object's shape, the mass (weight) is kept strictly the same for all Objects.

Figures 12, 13, 14, and 15 aim to capture the influence of the material pair on the moment when the Object starts to slip.

Figures 16, 17, and 18 aim to capture the influence of the gripping area geometry on the moment the Object starts to slip.

THE ANNALS OF "DUNAREA DE JOS" UNIVERSITY OF GALATI
FASCICLE IX. METALLURGY AND MATERIALS SCIENCE
Nº. 2 - 2025, ISSN 2668-4748; e-ISSN 2668-4756
Article DOI: https://doi.org/10.35219/mms.2025.2.03

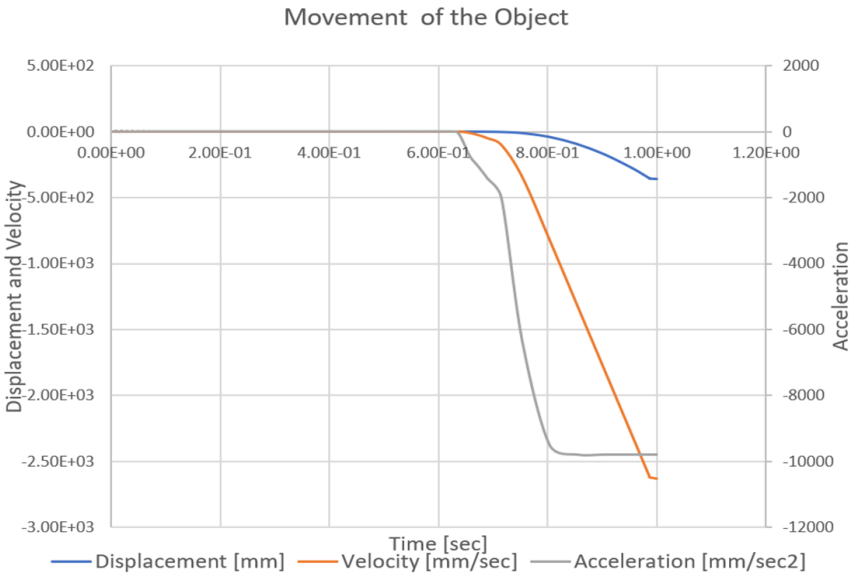

Fig. 10. *Displacement, Velocity and Acceleration for the Object*

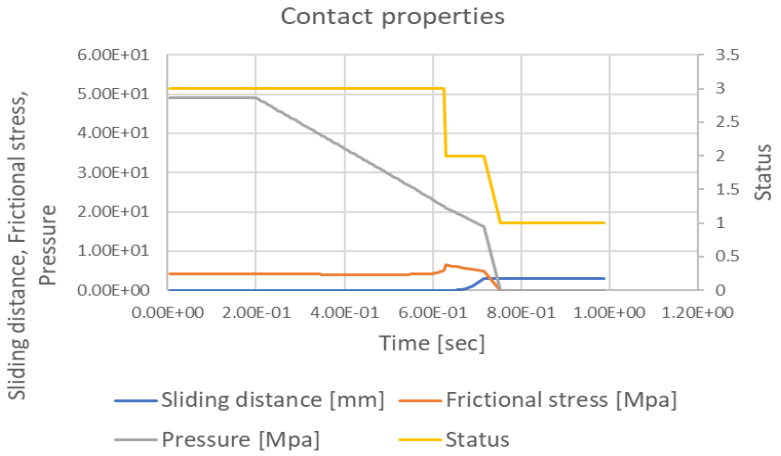

Fig. 11. *Contact properties*

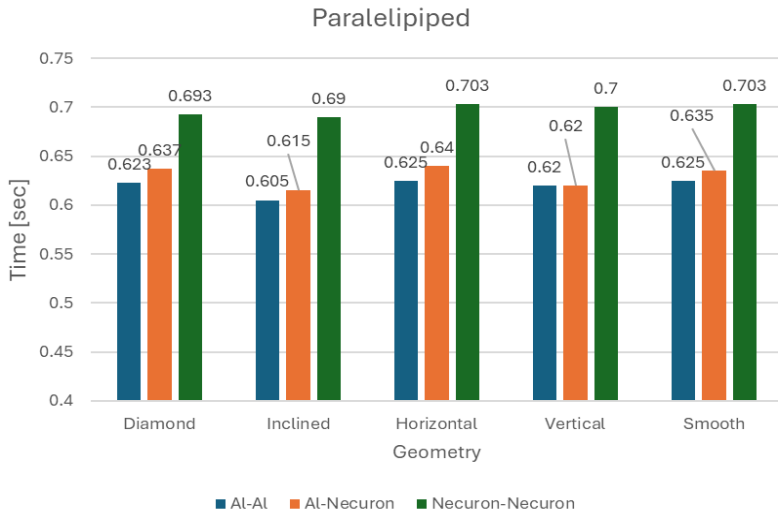

Fig. 12. *Moments in time when sliding initiates for the parallelepipedal Object*

THE ANNALS OF "DUNAREA DE JOS" UNIVERSITY OF GALATI
FASCICLE IX. METALLURGY AND MATERIALS SCIENCE
Nº. 2 - 2025, ISSN 2668-4748; e-ISSN 2668-4756
Article DOI: https://doi.org/10.35219/mms.2025.2.03

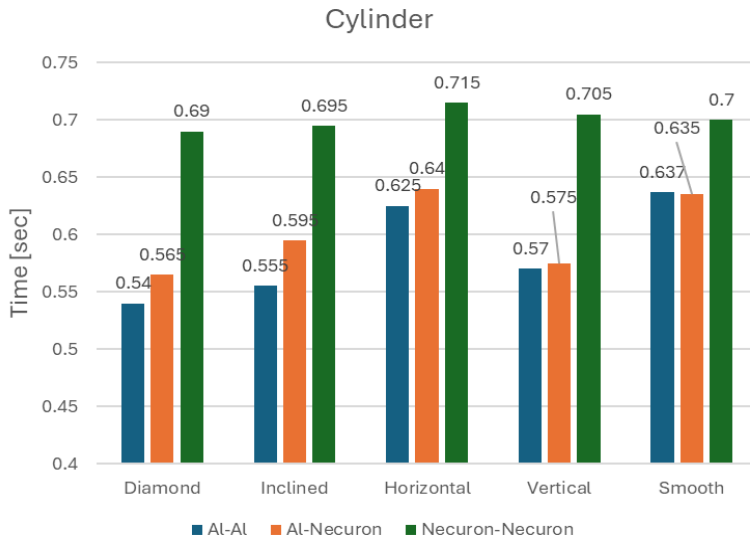

Fig. 13. *Moments in time when sliding initiates for the cylindrical Object*

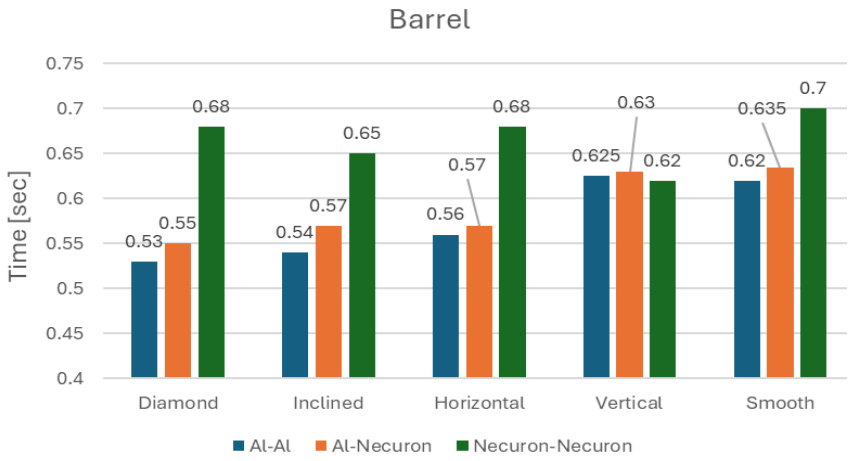

Fig. 14. *Moments in time when sliding initiates for the barrel Object*

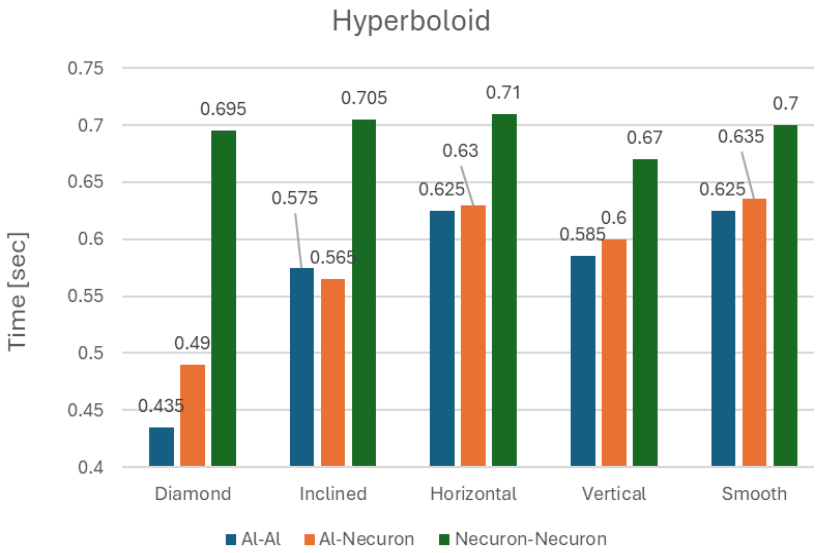

Fig. 15. *Moments in time when sliding initiates for the hyperboloidal Object*

THE ANNALS OF "DUNAREA DE JOS" UNIVERSITY OF GALATI
FASCICLE IX. METALLURGY AND MATERIALS SCIENCE
Nº. 2 - 2025, ISSN 2668-4748; e-ISSN 2668-4756
Article DOI: https://doi.org/10.35219/mms.2025.2.03

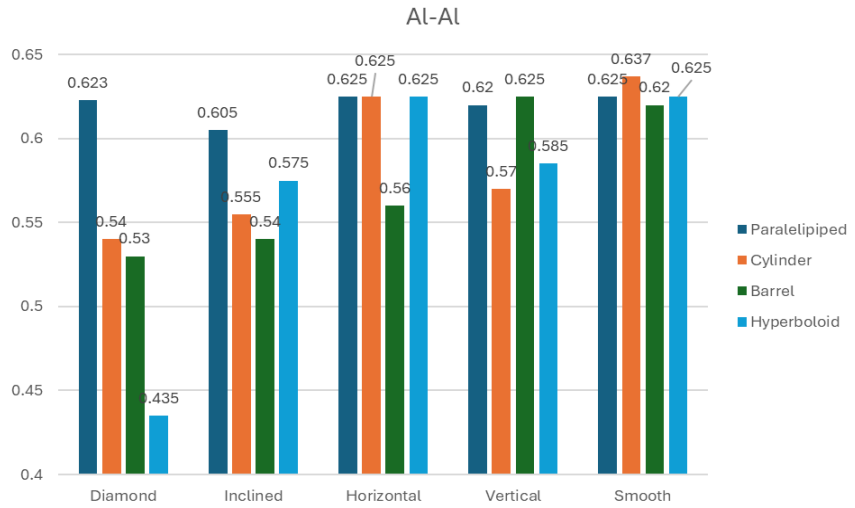

Fig. 16. *Moments in time when sliding initiates for the Al-Al pair of materials*

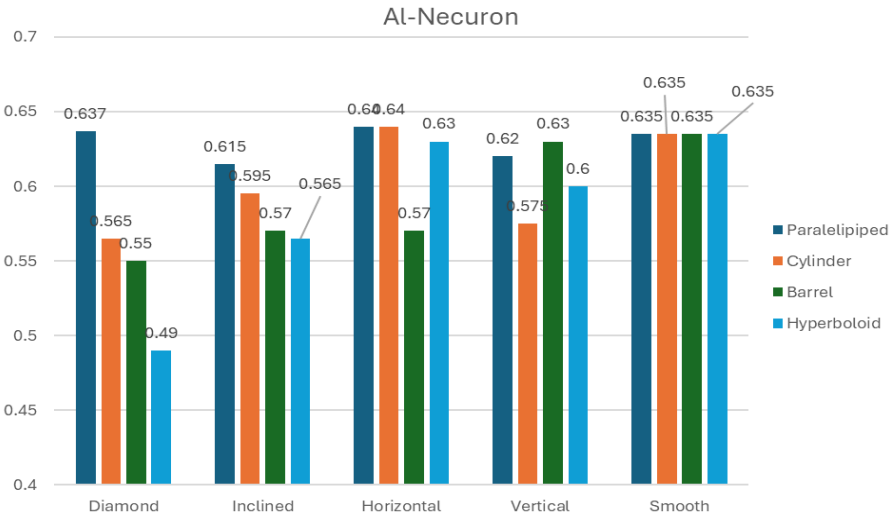

Fig. 17. *Moments in time when sliding initiates for the Al-Necuron pair of materials*

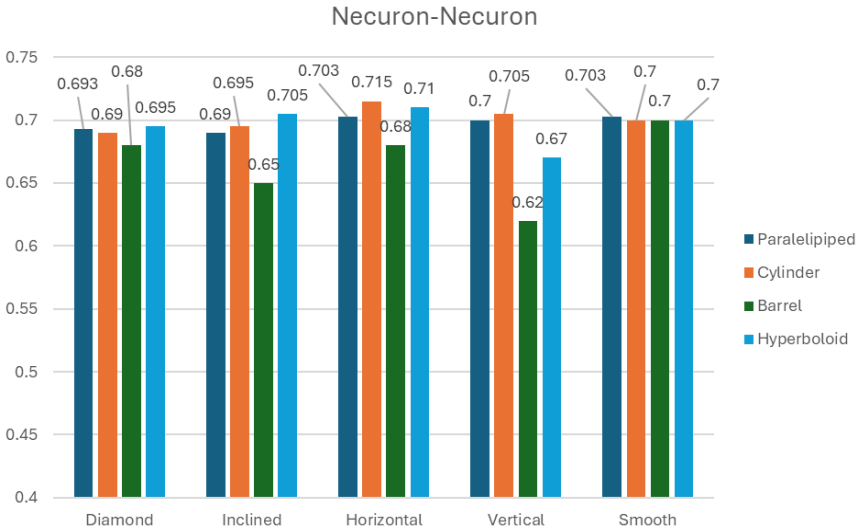

Fig. 18. *Moments in time when sliding initiates for the Necuron-Necuron pair of materials*

THE ANNALS OF "DUNAREA DE JOS" UNIVERSITY OF GALATI
FASCICLE IX. METALLURGY AND MATERIALS SCIENCE
Nº. 2 - 2025, ISSN 2668-4748; e-ISSN 2668-4756
Article DOI: https://doi.org/10.35219/mms.2025.2.03

7. Discussions and Conclusions

All the bar plots present on the vertical axis moments in time (expressed in seconds) when the grip is lost, and the Object starts to move. Greater values of time mean lower values for the gripping force necessary to keep the Object in a still position.

Keeping this in mind, we can make the following remarks on the influence of the pair of materials on the stability of the gripping:

- For all shapes of the Object (Figures 12-15), the best pair of materials (requiring less gripping force) is Necuron-Necuron;
- If we want to assess the relative differences between the values over time, we can see in Table 1, that while in the case of Necuron-Necuron versus Al-Al or Necuron-Necuron versus Al-Necuron the differences cover the range of 10%-49%, with the largest differences seen for the hyperboloid-shaped Object, in the case of Al-Al and Al-Necuron the values are significantly smaller (with a maximal value of 12 % in the case of the hyperboloidal-shaped Object);
- In all cases, the "worst" pair of materials is Al-Al.

Figures 16, 17 and 18 allow us to better compare, graphically, the influence that the shape of the Object, along with the geometry in the gripping area, have on the efficiency of the grip. We can therefore make the following remarks:

Table 1. *Relative errors (for sliding velocity)*

		1	2	3			
		Sliding velocity			Relative error [%]		
		Al-Al	Al-Nec	Nec-Nec	(3-1)/1	(3-2)/2	(2-1)/1
Parallelepiped	Diamond	0.623	0.637	0.693	11.2%	8.8%	2.2%
	Inclined	0.605	0.615	0.69	14.0%	12.2%	1.7%
	Horizontal	0.625	0.64	0.703	12.5%	9.8%	2.4%
	Vertical	0.62	0.62	0.7	12.9%	12.9%	0.0%
	Smooth	0.625	0.635	0.703	12.5%	10.7%	1.6%
Cylinder	Diamond	0.54	0.565	0.69	27.8%	22.1%	4.6%
	Inclined	0.555	0.595	0.695	25.2%	16.8%	7.2%
	Horizontal	0.625	0.64	0.715	14.4%	11.7%	2.4%
	Vertical	0.57	0.575	0.705	23.7%	22.6%	0.9%
	Smooth	0.637	0.635	0.7	9.9%	10.2%	-0.3%
Barrel	Diamond	0.53	0.55	0.68	28.3%	23.6%	3.8%
	Inclined	0.54	0.57	0.65	20.4%	14.0%	5.6%
	Horizontal	0.56	0.57	0.68	21.4%	19.3%	1.8%
	Vertical	0.625	0.63	0.62	-0.8%	-1.6%	0.8%
	Smooth	0.62	0.635	0.7	12.9%	10.2%	2.4%
Hyperboloidal	Diamond	0.435	0.49	0.695	59.8%	41.8%	12.6%
	Inclined	0.575	0.565	0.705	22.6%	24.8%	-1.7%
	Horizontal	0.625	0.63	0.71	13.6%	12.7%	0.8%
	Vertical	0.585	0.6	0.67	14.5%	11.7%	2.6%
	Smooth	0.625	0.635	0.7	12.0%	10.2%	1.6%

- For the Al-Al pair of materials we observe that:
  - the biggest differences in time are registered for the diamond geometry of the gripping area (with differences up to 43%);
  - for the other geometries of the gripping area, the differences are smaller but still significant;
  - for the parallelepiped-shaped Objects, the differences in time are small regardless of the gripping regions geometry;
  - these differences are more pronounced for the other cases;
  - for the smooth geometry of the gripping area, these differences are very small;
  - as expected, the barrel-shaped Object is the most difficult to keep in a still position (with an exception for the diamond and vertical geometry of the gripping area. In this case, it seems that this geometry allows a better contact area between the Object and the gripper).
- For the Al-Necuron pair of materials we observe that:
  - for the diamond geometry of the gripping area, the trend encountered in the case of Al-Al pair

THE ANNALS OF "DUNAREA DE JOS" UNIVERSITY OF GALATI
FASCICLE IX. METALLURGY AND MATERIALS SCIENCE
No. 2 - 2025, ISSN 2668-4748; e-ISSN 2668-4756
Article DOI: https://doi.org/10.35219/mms.2025.2.03

of materials is also visible, although with smaller amplitude;

- in the case of the smooth gripping geometry, there is no difference between the four Object geometries;
- we can appreciate that the pairs Al-Al and Al-Necuron behave quite similarly;
- as expected, again, the barrel-shaped Object is the most difficult to keep in a still position (with an exception for the diamond and vertical geometry of the gripping area). In this case, it seems that this geometry allows a larger contact area between the Object and the gripper - this confirms the results for Al-Al pair of materials.

- For the Necuron-Necuron pair of materials we observe that:

- for the diamond geometry of the gripping area, in this case, there are almost no significant differences between the four Object geometries;
- again, for the smooth gripping geometry there is no difference between the four Object geometries;
- in general, with a small exception for the vertical geometry of the gripping area, the values for the moments in time when the Object starts to move are smaller;
- the barrel-shaped object is again the most difficult case, this time with no exception.

As general conclusions on what geometry is better for different types of Objects, we can formulate the following statements:

- For the parallelipiped Object:

- for all pairs of materials, there are few differences between the five geometries of the gripping region;
- the Necuron-Necuron pair of materials provides the best performances.

- For the cylindrical Object:

- for the Al-Al and Al-Necuron pairs of materials, horizontal and smooth geometries provide the best results;
- for the Necuron-Necuron pair of materials, horizontal geometry provides the best results.

- For the barrel-shaped object:

- for all pairs of materials, horizontal and smooth geometries provide the best results.

- For the hyperboloidal Object:

- for the Al-Al and Al-Necuron pairs of materials, horizontal and smooth geometries provide the best results;
- for Necuron-Necuron, there are small differences between the five geometries.

Finally, we make the observation that for the hyperboloidal Object, due to the shape, the contact region induces numerical instabilities in the FEA approach.

References

[1]. Dharbaneshwer S. J., Subramanian S. J., Kohlhoff K., *Robotic grasp analysis using deformable solid mechanics*, Meccanica, vol. 54, p. 1767-1784, 2019.

[2]. Turrell Y. N., Li F.-X., Wing A. M., *Estimating the minimum grip force required when grasping objects under impulsive loading conditions*, Behavior Research Methods, Instruments, & Computers, vol. 33(1), p. 38-45, 2001.

[3]. Sathishkumar A., *et al.*, *Design and Analysis of a Multi Fingered Gripper for Grasping Irregular Objects*, International Research Journal of Engineering and Technology (IRJET), vol. 04(3), 2017.

[4]. Hao Y., *et al.*, *Modeling and experiments of a soft robotic gripper in amphibious environments*, International Journal of Advanced Robotic Systems, May-June, p. 1-12, DOI: 10.1177/1729881417707148, 2017.

[5]. Miller A. T., Allen P. K., *Examples of 3D Grasp Quality Computations*, Proceedings of the IEEE International Conference on Robotics & Automation, Detroit, Michigan, May 1999.

[6]. Lu Q., *et al.*, *An Origami-Inspired Variable Friction Surface for Increasing the Dexterity of Robotic Grippers*, IEEE Robotics and Automation Letters, vol. 5(2), p.2538-2545, DOI: 10.1109/LRA.2020.2972833, 2020.

[7]. Sahbani A., El-Khoury S., Bidaud P., *An overview of 3D object grasp synthesis algorithms*, Robotics and Autonomous Systems, vol. 60 (3), p. 326-336, 2012.

[8]. Ferrari C., Canny J., *Planning Optimal Grasp*, Proceedings IEEE International Conference on Robotics and Automation, DOI: 10.1109/ROBOT.1992.219918, May 1992.

[9]. Romeo R. A., *et al.*, *Slippage Detection with Piezoresistive Tactile Sensors*, Sensors, vol. 17(8), p. 1844, DOI: 10.3390/s17081844, 2017.

[10]. Hu Al., Peachey B., *Redesigning an Experiment to Determine the Coefficient of Friction*, Journal of Emerging Investigators, June 2016.

[11]. Kapucu S., *A simple experiment to measure the maximum coefficient of static friction with a smartphone*, Phys. Educ. 53, 053006 (3pp), 2018.

[12]. Dickey R. D. I., Jackson R. L., Flowers G. T., *Measurements of the Static Friction Coefficient Between Tin Surfaces and Comparison to a Theoretical Model*, Journal of Tribology, vol. 133 (3), DOI: 10.1115/1.4004338, 2011.

[13]. Lee C-H., Polycarpou A. A., *Static Friction Experiments and Verification of an Improved Elastic-Plastic Model Including Roughness Effects*, Journal of Tribology, vol. 129(4), DOI: 10.1115/1.2768074, 2007.

[14]. Metcalfe A., *et al.*, *Statistics in Engineering: With Examples in MATLAB® and R*, Second Edition, Chapman and Hall/CRC, New York, 2019.

[15]. Groß T., *Technische Produktdokumentation: Detaillierungsfunktionen mit Siemens NX*, 978-3-658-28266-0, Springer Fachmedien Wiesbaden, Springer Vieweg, 2020.

[16]. Tickoo S., *Siemens NX 12.0 for Designers*, 11th Edition, 1640570128, 9781640570122, CADCIM Technologies, 2018.

[17]. ***, *ANSYS Inc. Theory Reference*, Canonsburg: SAS IP Inc.

THE ANNALS OF "DUNAREA DE JOS" UNIVERSITY OF GALATI
FASCICLE IX. METALLURGY AND MATERIALS SCIENCE
No. 2 - 2025, ISSN 2668-4748; e-ISSN 2668-4756
Article DOI: https://doi.org/10.35219/mms.2025.2.04

ON THE OPTIMIZATION OF MACHINED VSD POSITION FOR REPAIRED PIPES

Ionuţ LAMBRESCU
Universitatea Petrol-Gaze din Ploieşti, Bd. Bucureşti 39, Ploieşti, Romania
e-mail: ilambrescu@upg-ploiesti.ro

ABSTRACT

To be kept in use, pipelines with Volumetric Surface Defects (VSDs) must be evaluated and, if necessary, repaired. The first step in the repair process is machining the defect area. In all cases, the machined defect has a rectangular shape, with edges parallel/perpendicular to the pipe axis. We propose a novel approach: the VSD is scanned, the image is then processed using segmentation techniques, the VSD contour is detected, and finally, a family of rectangles with minimal area enclosing the VSD is defined. After that, a Finite Element Analysis is performed for each machined VSD, and an optimal case is selected.

KEYWORDS: pipes, volumetric defects, optimization

1. Introduction

The problem of pipelines with Volumetric Surface Defects (VSDs) is of great interest, since accidents involving pipelines transporting flammable or explosive fluids can have very serious consequences.

The general approach is to analyse the VSD and assess if the pipeline can be accepted as it is and allowed to continue operating, or it is necessary to apply a repair process that will enable the pipeline to remain in use for a specified period of time [1-4]. The repair process involves a machining phase, during which material in the area of the VSD is removed, followed by a repair phase, during which a material (the so-called filler) is used to fill the machined VSD, and the pipe is wrapped with a multilayer composite material [5].

In the literature that addresses this topic, the machined VSD is typically of rectangular shape, with the edges of the rectangle oriented parallel/perpendicular to the pipeline's axis [6].

In a previous paper, the author analysed the influence of the machined rectangular VSD on the stress and displacement distribution. The conclusion was that there exists a position of the machined VSD that produces a more favourable stress distribution [2].

The present paper aims to continue this analysis, this time starting from a real VSD, for which the objective is to find the most favourable dimensions and orientation of the rectangular machined VSD. The stages of the process are described in Figure 1.

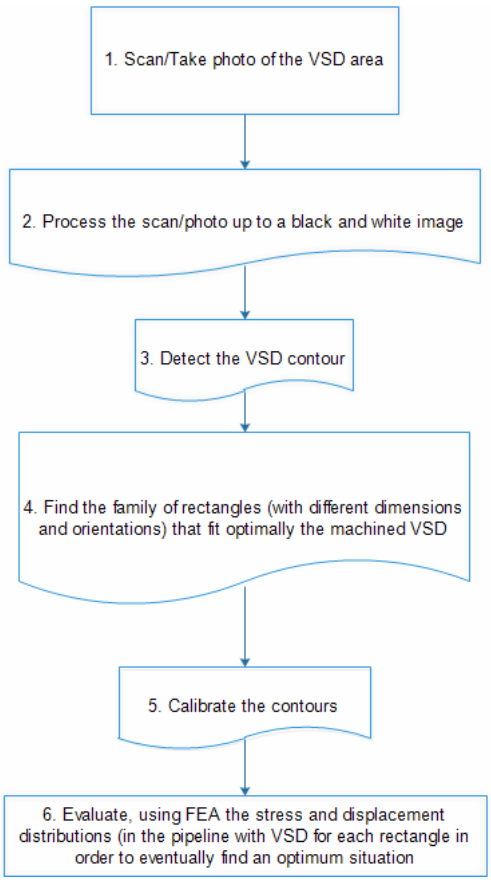

Fig. 1. *Stages of the proposed workflow*

THE ANNALS OF "DUNAREA DE JOS" UNIVERSITY OF GALATI
FASCICLE IX. METALLURGY AND MATERIALS SCIENCE
N°. 2 - 2025, ISSN 2668-4748; e-ISSN 2668-4756
Article DOI: https://doi.org/10.35219/mms.2025.2.04

The first four stages of the workflow imply, apart from scanning [7, 8] or taking a picture of the area of the pipeline with a VSD, writing a script that will accomplish stages 2, 3, and 4 in the workflow.

Stage 5 involves the calibration process, since the rectangles resulting from stage 4 have dimensions expressed in pixels. These dimensions must be converted to dimensions expressed in millimeters (mm). This is the process we call calibration. Details on how this is done will be given later in the paper.

Stage 6 involves performing finite elements analysis for each scenario (a scenario corresponds to a rectangle with specific dimensions and orientation). In the end, we will ultimately obtain an optimal solution -that is, the case with the smallest values for stresses.

2. Image processing

Figure 2.a presents an image obtained through a 3D scanning process (the image shows only the region containing the VSD, which has been isolated from a pipeline with an outer diameter of 508 mm and a wall thickness of 10 mm). The scan was performed using an HP 3D Structured Light Scanner Pro 3 [9].

The image was converted to black and white (bw) format, as presented in Figure 2.b. All image processing was performed in Matlab [10, 11].

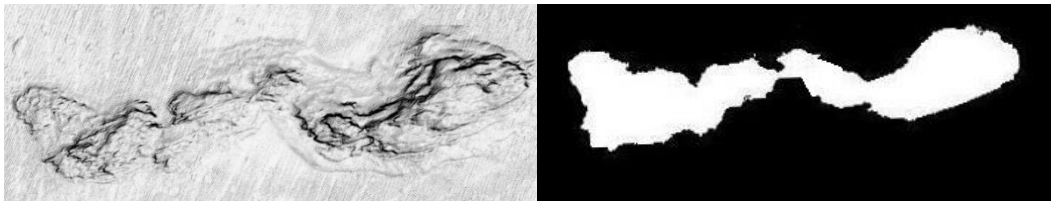

a) Initial scanned image *b) Processed image (bw)*

Fig. 2. *Images with VSD*

2.1. Determination of the family of rectangles

The bw image serves as an input for the process of determining a family of rectangles that will fit (enclose) the boundary of the VSD. Each rectangle will fit the boundary of the VSD and will have edges parallel/perpendicular to variable directions that pass through the centroid of the VSD area. Essentially, this results in a family of rectangles that rotate around a central point. This point is the centroid of the VSD area, and it is identified by our application using image segmentation techniques [12, 13]. For better understanding see Figure 3.

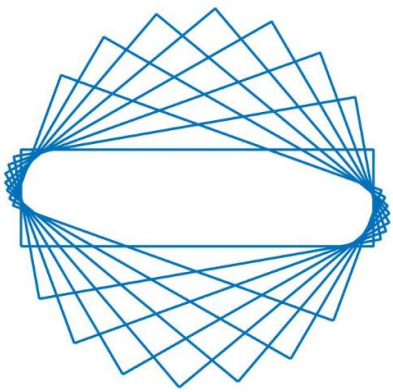

Fig. 3. *Family of rectangles*

In order to better understand the following explanations, Figure 4 presents the VSD as it appears on the pipeline. In the same image, a bounding rectangle is shown at a position tilted by 10 degrees.

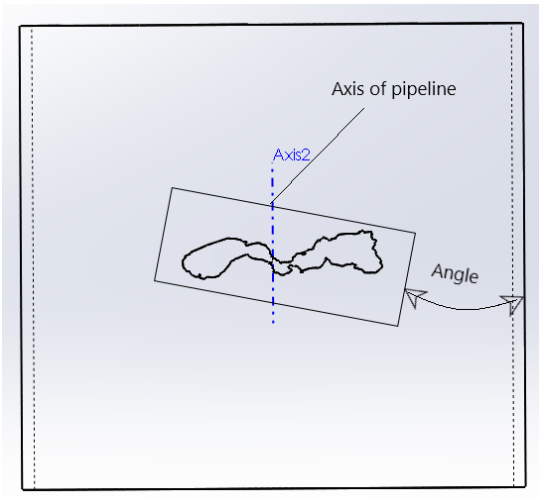

Fig. 4. *VSD and a bounding rectangle*

Figure 5 presents the first 4 bounding boxes for the VSD shown in Figure 2, starting from a direction tilted at 0 degrees and ending with one tilted at 30 degrees.

It should be noted that when the bounding rectangles were generated, we applied a covering

THE ANNALS OF "DUNAREA DE JOS" UNIVERSITY OF GALATI
FASCICLE IX. METALLURGY AND MATERIALS SCIENCE
N°. 2 - 2025, ISSN 2668-4748; e-ISSN 2668-4756
Article DOI: https://doi.org/10.35219/mms.2025.2.04

tolerance of 7%. This was necessary since some of the calculations performed during the process produced non-integer values, while coordinates within the image must be integer values. This is a source of small errors that must be compensated.

The VSD presented in Figure 2 also has a special characteristic. It is placed on the pipeline such that its minimum bounding box (the minimum bounding box is a property of the VSD area, determined using image segmentation techniques) has edges that are parallel or perpendicular to the pipeline's axis. The dimensions and position of the minimum bounding box are intrinsic properties of the VSD area as an image region, while for all other rectangles, edge orientation is constrained. For these rectangles, the dimensions are resulting parameters, determined after the orientation is fixed.

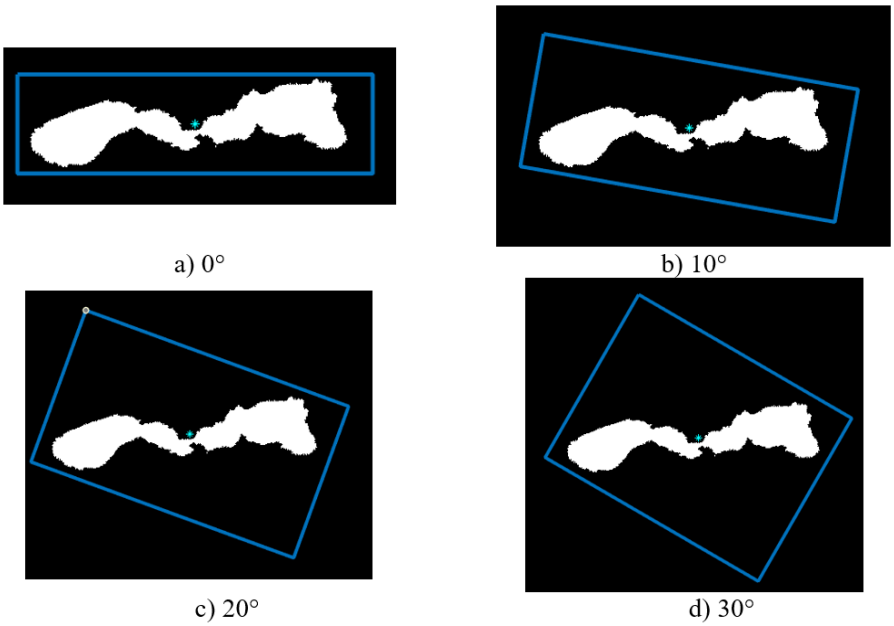

a) 0° b) 10° c) 20° d) 30°

... and other 4 positions up to 70°

Fig. 5. *Bounding rectangles*

3. Finite Element Analysis

For the eight rectangles we obtained (from 0 degrees to 70 degrees, in 10-degree steps), we performed a finite element analysis in order to determine if we can identify a most favourable configuration (in terms of stress values) [14-19].

The analysis was performed using Ansys Mechanical [20].

As shown in Figure 6, each rectangle serves as the starting point for the machining of the VSD. The machined VSDs include fillet radii and depths that depend on the depth of the original VSD. In our case, the VSD depth was 7.5 mm.

The results obtained for the VSD depicted in Figure 2 are presented in Figure 7. For each orientation of the machined VSD, we present the values for Von Mises stress, circumferential stress, and radial displacements, respectively.

As can be seen in Figure 7, the values for all the considered parameters reach their minimum for the bounding rectangle tilted at 0 degrees (it is in fact the minimum bounding box of the VSD contour). At this stage, we emphasize that the relative variation for all three parameters is significant: 55% for Von Mises stress, 45% for circumferential stress, and 72% for radial displacement, respectively.

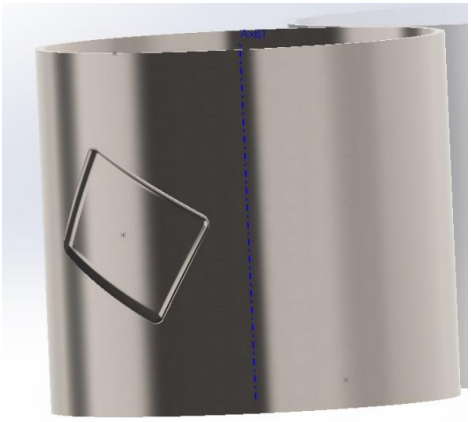

Fig. 6. *Machined VSD for one of the analysed positions*

THE ANNALS OF "DUNAREA DE JOS" UNIVERSITY OF GALATI
FASCICLE IX. METALLURGY AND MATERIALS SCIENCE
No. 2 - 2025, ISSN 2668-4748; e-ISSN 2668-4756
Article DOI: https://doi.org/10.35219/mms.2025.2.04

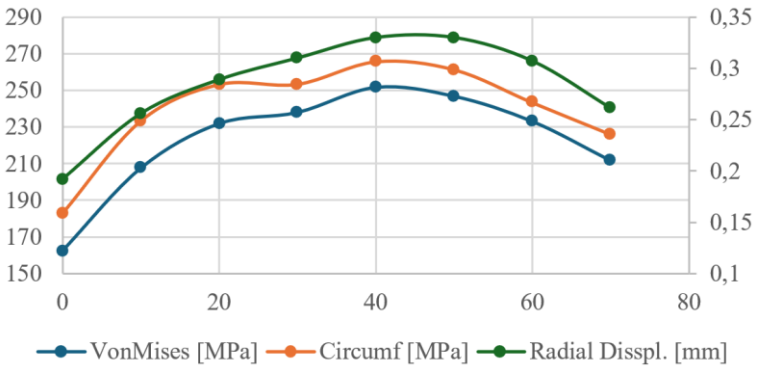

Fig. 7. *Comparison between positions of the machined VSDs*

Because the first VSD considered had a particular orientation on the pipeline, we also analysed another VSD. Its position on the pipeline is presented in Figure 8.a.

In Figures 8.b-f, one can see the bounding rectangles obtained with our code, again for angles ranging from 0 degrees to 70 degrees, in 10-degrees increments.

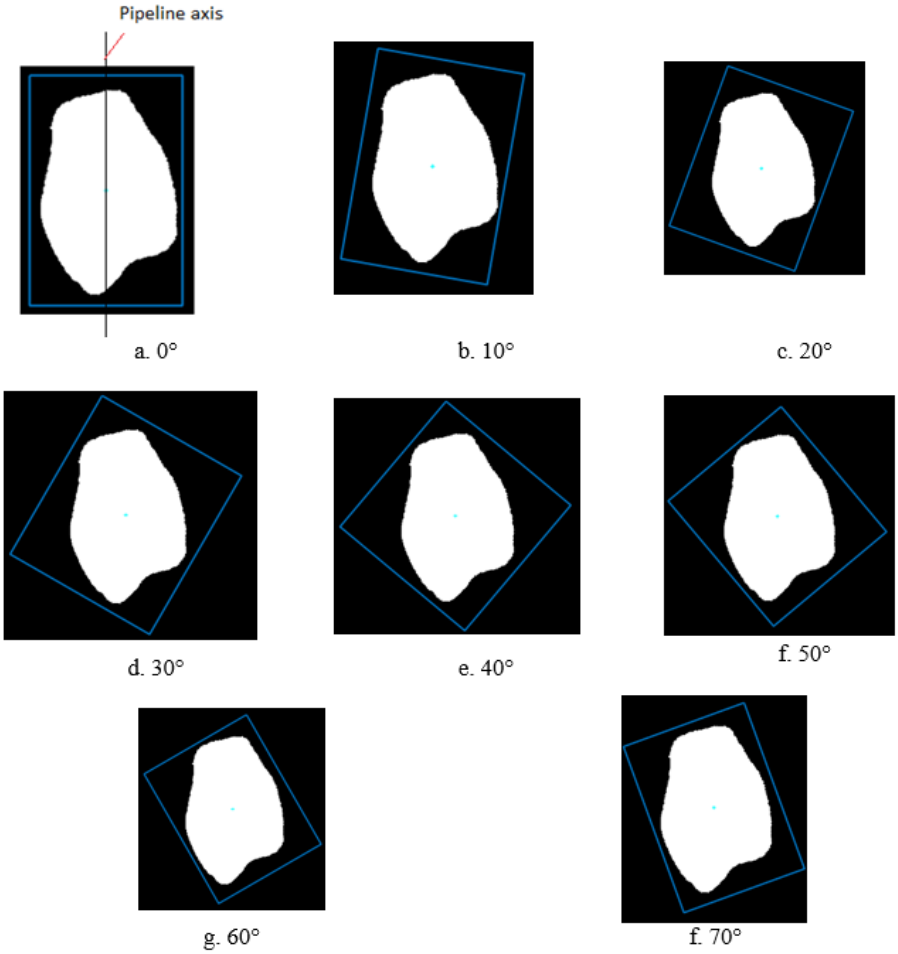

Fig. 8. *Bounding rectangles for another VSD*

In this case, the results are presented in Figure 9. This time it is obvious that for tilting angles of 40, 50, and 60 degrees, one obtains significantly lower values for all the three considered parameters.

THE ANNALS OF "DUNAREA DE JOS" UNIVERSITY OF GALATI
FASCICLE IX. METALLURGY AND MATERIALS SCIENCE
Nº. 2 - 2025, ISSN 2668-4748; e-ISSN 2668-4756
Article DOI: https://doi.org/10.35219/mms.2025.2.04

The relative variation of these parameters over the angle range is as follows: 30.5% for Von Mises stress, 34.1% for circumferential stress, and 9% for radial displacement respectively

Another interesting observation is that by modifying the tilting angle, the locations of maximum stress values (Von Mises or circumferential) is registered in different VSD areas. Figure 10.a for example presents the Von Mises stress distribution (for the second VSD) with a bounding rectangle tilted at 0 degrees (the minimum bounding box), while Figure 10.b shows the same parameter for a bounding rectangle tilted at 40 degrees. It is clear that the region with high stress values is smaller in the latter case.

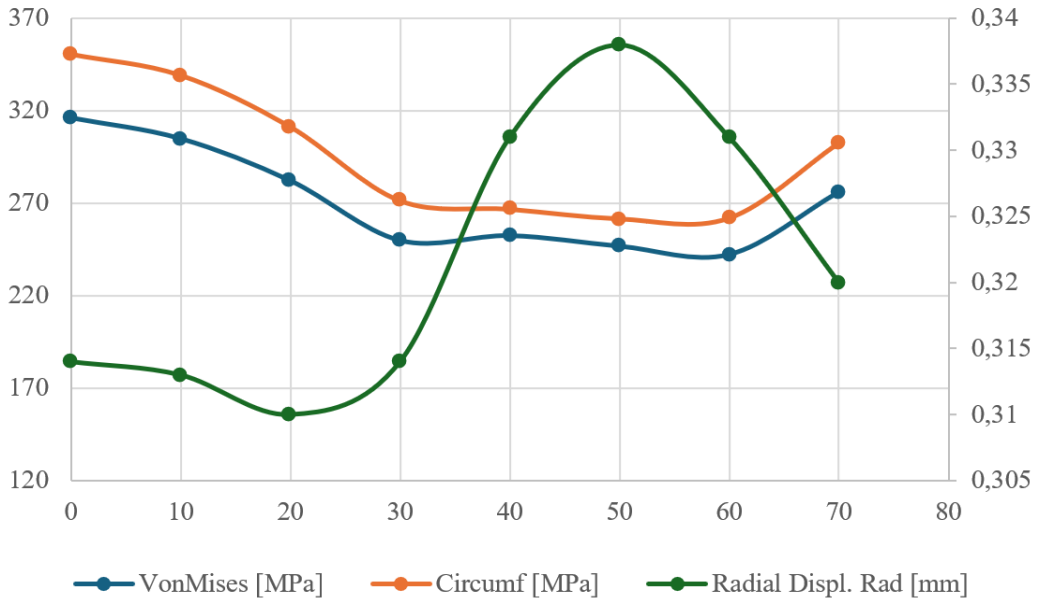

Fig. 9. *Comparison between positions of the machined VSDs from Figure 8*

Figure 11 presents the variation of the three parameters with the tilting angle, with two curves added. These curves are obtained for a value of the fillet angle of the machined VSD of 20 mm (instead of 15 mm). We can see that for tilting angles of 40 and 50 degrees, there are relative differences of 3%.

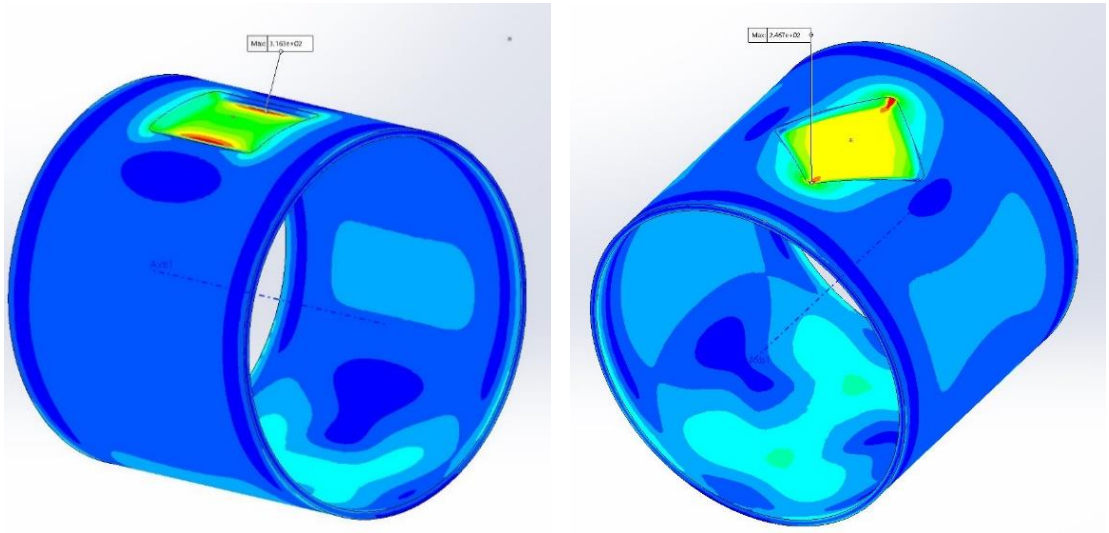

a) Von Mises stress 0 degrees *b) Von Mises stress 40 degrees*

Fig. 10. *Comparison between positions of the maxima Von Mises stress areas*

THE ANNALS OF "DUNAREA DE JOS" UNIVERSITY OF GALATI
FASCICLE IX. METALLURGY AND MATERIALS SCIENCE
Nº. 2 - 2025, ISSN 2668-4748; e-ISSN 2668-4756
Article DOI: https://doi.org/10.35219/mms.2025.2.04

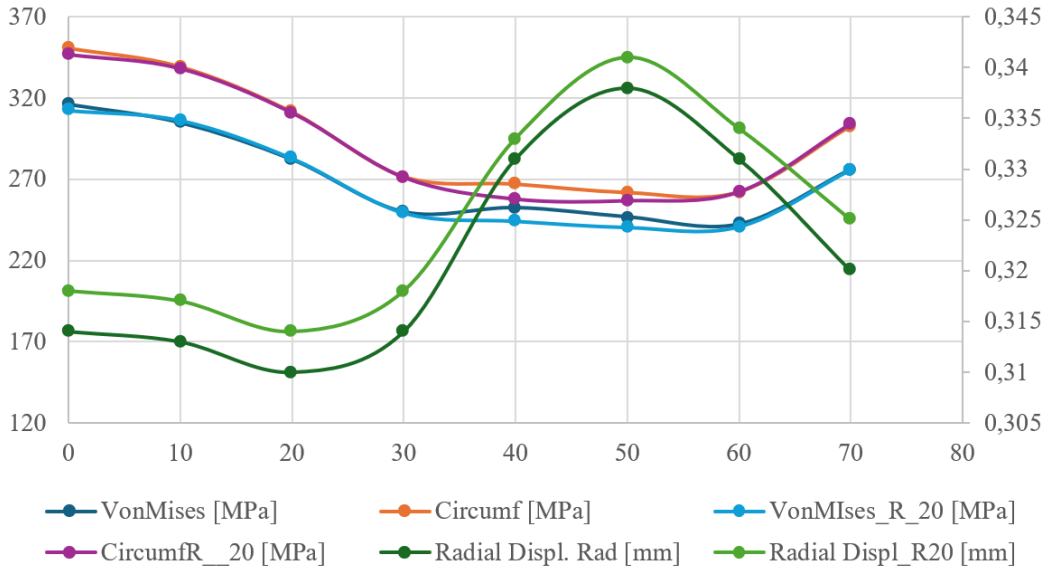

Fig. 11. *Comparison between positions of the machined VSDs from Fig. 8 including cases with fillet radius of 20 mm*

4. Conclusions

Practically all studies [1, 19, 21, 22] (and the references can be extended) dealing with repaired pipes containing VSDs consider the machined VSD to be rectangular, with edges parallel/perpendicular to the pipe axis. However, there are cases where, due to the VSD shape, the resulting machined area becomes very large, this implying not only the fact that the pipe is weakened, but also the time for machining the VSD is increasing. What the author is proposing is a method to identify the optimal rectangular shape for the machined VSD – one that circumscribes the unprocessed defect but has edges inclined to the pipe axis. The best machined VSD is selected through finite element analysis of multiple VSD orientations. The optimal rectangle is the one that "produces" the most favourable stress, strain, or displacements in the pipe with machined VSD. The analysis performed showed that both the dimension and position of the machined VSD significantly influenced the stress/strain distribution in the pipe (with differences of up to more than 30% for Von Misses stresses).

Furthermore, the shape and orientation of the bounding rectangle also influence the area where the stress exhibits maximum values (see Fig. 10). This detail is of paramount importance, as it can be correlated with the fillet radius applied at the VSD bottom to help identify regions with high failure risk.

The proposed method can be sped up using parametrization techniques in generating the geometric model of the pipe with machined VSD.

Because the finite element analysis performed is static structural (linear), the overall duration of the process is reduced.

We believe that the advantages offered by the proposed method, in terms of increased repaired pipe resistance and reduced machining time, makes this research valuable to professionals working in the field.

References

[1]. Yeom K. J., *et al.*, *Integrity Assessment of a Corroded API X70 Pipe with a Single Defect by Burst Pressure Analysis*, Engineering Failure Analysis, vol. 57, p. 553-561, November 2015.
[2]. Lambrescu I., Dinita A., Minescu M., *About the Influence of the Corrosion Defect Geometry on Repaired Pipes Stress Distribution*, J. Pressure Vessel Technol., 143(1), 011802, /doi.org/10.1115/1.4047877, Feb 2021.
[3]. Chebakov M. J., *et al.*, *Experimental and Numerical Research on Renovated Pipeline Prototype with Durface Defect, Non-destructive Testing and Repair of Pipelines*, E. N. Barkanov, A. Dumitrescu, I. A. Parinov, eds. Springer International Publishing AG, Cham, Switzerland, p. 353-368, 2018.
[4]. Su C.-I., Li X., Zhou J., *Failure Pressure Analysis of Corroded Moderate-to-High Strength Pipelines*, China Ocean Engineering, vol. 30, issue 1, p. 69-82.
[5]. ***, *ISO 24817:2015. Petroleum, petrochemical and natural gas industries — Composite repairs for pipework — Qualification and design, installation, testing and inspection*.
[6]. Barkanov E. N., Dumitrescu A., Parinov I. A., *Non-destructive Testing and Repair of Pipelines*, Springer International Publishing AG, Cham, Switzerland.
[7]. Lambrescu I., Dinita A., Minescu M., *Considerations on the Evaluation and Management of Volumetric Surface Defects on Pipelines Using 3D Scanning and Finite Element Analysis*, Revista de chimie, 71 (4), p. 19-28, 2020.
[8]. Lambrescu I., Minescu M., Dinita A., *Implementing of 3D Scanning Techniques in the Analytical and Numerical Assessment of Pipelines with Volumetric Surface Defects*, Revista de Chimie, 70, no. 12, 2019.

[9]. ***, https://support.hp.com/us-en/product/details/hp-3d-structured-light-scanner/model/14169439.
[10]. Song Y. Q., Gao C. Y., *Application of MATLAB on Moire image processing*, Proceedings of the 5th International Conference on Nonlinear Mechanics, p. 854-856, 2007.
[11]. Magrab E. B., *et al.*, *An Engineer's Guide to MATLAB, 3e: with Applications from Mechanical, Aerospace, Electrical, and Civil Engineering*, Prentice Hall, 2011.
[12]. Tewari P., Surbhi P., *Evaluation of some recent Image segmentation method's*, 3rd International Conference on Computing for Sustainable Global Development (INDIACom), Proceedings of the 10th Indiacom, 3rd International Conference on Computing for Sustainable Global Development, p. 3741-3747, 2016.
[13]. Song Y. H., Yan H., *Image Segmentation Techniques Overview*, Asia Modelling Symposium (AMS) / 11th International Conference on Mathematical Modelling and Computer Simulation, p. 103-107, 2017.
[14]. Jungyeom K., *et al.*, *Integrity assessment of a corroded API X70 pipe with a single defect by burst pressure analysis*, Engineering Failure Analysis, vol. 57, p. 553-561, November 2015.
[15]. Zienkiewicz O. C., Taylor R. L., *Finite Element Method for Solid and Structural Mechanics*, Sixth Edition. Elsevier BH, Oxford, UK, 2006.
[16]. Nasedkina A. A., *et al.*, *Static Finite Element Analysis of a Pipeline with Volumetric Surface Defects Using MPC Approach*, International Conference on Physics and Mechanics of New Materials and their Applications (PHENMA 2015), At Azov, Russia.
[17]. Chiodo M. S., Ruggieri C., *Failure assessments of corroded pipelines with axial defects using stress-based criteria: Numerical studies and verification analyses*, International Journal of Pressure Vessels and Piping, 86, p. 164-176, 2009.
[18]. Liu H., Khan F., Thodi P., *Revised burst model for pipeline integrity assessment*, Engineering failure analysis, 80, p. 24-38, 2017.
[19]. da Costa Matos H. S., *et al.*, *Failure Analysis of Corroded Pipelines Reinforced with Composite Repair Systems*, Engineering Failure Analysis, vol. 59, p. 223-236, 2016.
[20]. *, *ANSYS – Finite Element Analysis, Release 19.0 User Guide*, 2018.
[21]. Lim K. S., *et al.*, *Behaviour of Steel Pipelines with Composite Repairs Analyzed using Experimental and Numerical Approaches*, Thin-Walled Structures 139, p. 321-333, 2019.
[22]. Noor N., *et al.*, *An Overview of Corroded Pipe Repair Techniques Using Composite Materials*, International Journal of Chemical, Molecular, Nuclear, Materials and Metallurgical Engineering. vol. 10, no. 1, p. 19-25, 2016.

THE ANNALS OF "DUNAREA DE JOS" UNIVERSITY OF GALATI
FASCICLE IX. METALLURGY AND MATERIALS SCIENCE
Nº. 2 - 2025, ISSN 2668-4748; e-ISSN 2668-4756
Article DOI: https://doi.org/10.35219/mms.2025.2.05

FROM MECHANICAL TESTING TO DECISION MAKING: SELECTING A STRUCTURAL ADHESIVE USING THE WEIGHTED SUM METHOD

Andreea ȚÎNTATU
Faculty of Mechanics and Technology, National University of Science and Technology Politehnica Bucharest, Bucharest, 060042, Romania
e-mail: andreea.tintatu@upb.ro

ABSTRACT

The selection of structural adhesives in engineering applications demands a robust, transparent, and replicable methodology, especially when performance and reliability are critical. This study introduces a practical, scalable approach based on the Weighted Sum Method (WSM), a form of Multi-Criteria Decision Analysis (MCDA), to assist in the objective selection of adhesives. The novelty of this research lies in demonstrating that WSM can serve as an industrially applicable decision-making tool that translates mechanical testing data into clear, replicable selection criteria. Using experimental data from modified Arcan tests, the method provides a structured framework that can be extended to other types of tests and applications. This facilitates transparent, criterion-driven adhesive selection aligned with real-world constraints, offering engineers a powerful tool that supports consistent, informed, and reproducible decisions.

KEYWORDS: structural adhesives, mechanical test, decision criteria, WSM method

1. Introduction

In modern engineering applications, bonded assemblies have emerged as a crucial structural solution, offering significant advantages over traditional mechanical assembly. These advantages include improved stress distribution, reduced weight, and enhanced fatigue resistance. Structural adhesives are at the core of this advancement, enabling the reliable joining of dissimilar materials under complex loading conditions. Consequently, understanding and predicting the mechanical behavior of bonded joints is essential for ensuring the durability and performance of assembled structures in critical fields such as aerospace, automotive, and marine engineering [1].

The mechanical performance of an adhesive can be characterized at two distinct levels: as a bulk material and as part of a functional bonded joint. Bulk adhesive specimens provide an effective means for intrinsic material characterization, isolating the adhesive from substrate interactions and interface effects [2]. Standard uniaxial tensile (EN ISO 527-2), compression (ASTM D695), and shear tests [3-4] are commonly employed to determine fundamental properties such as Young's modulus, yield stress, and ultimate strength. However, these tests often fail to capture the complex stress states and degradation phenomena that occur within a bonded joint.

In practical assemblies, adhesives are rarely subjected to pure stress states; instead, they often face multi-axial loading and environmental influences, such as humidity and temperature variations. To address these complexities, test configurations that simulate real-world conditions are indispensable. Among the various test setups, the modified Arcan fixture has gained prominence due to its capacity to apply a wide range of loading angles—ranging from pure shear to pure tension or compression—by simply altering the orientation of the device relative to the testing machine [2, 5]. This versatility makes the Arcan method particularly suitable for robust mechanical characterization, especially when studying the coupling of mechanical loading and environmental effects.

The modified Arcan device offers several improvements over standard fixtures. Firstly, it facilitates uniform stress distribution within the adhesive layer, minimizing the effect of edge-induced stress concentrations commonly encountered in lap-

THE ANNALS OF "DUNAREA DE JOS" UNIVERSITY OF GALATI
FASCICLE IX. METALLURGY AND MATERIALS SCIENCE
Nº. 2 - 2025, ISSN 2668-4748; e-ISSN 2668-4756
Article DOI: https://doi.org/10.35219/mms.2025.2.05

shear tests [6-7]. Secondly, its ability to simulate multi-axial stress states enables a more comprehensive understanding of adhesive performance under realistic service conditions [8-9]. Finally, it allows precise parameter calibration for advanced constitutive models if needed [10].

Despite these experimental advancements, the adhesive selection process in industry remains challenging due to the multitude of performance criteria, from mechanical strength to environmental resistance and ease of application. While empirical testing provides valuable data, the final adhesive choice must consider multiple, sometimes conflicting, criteria that align with project-specific requirements. As such, the integration of a structured decision-making framework becomes necessary.

To support objective adhesive selection, decision-making tools such as Multi-Criteria Decision Analysis (MCDA) methods have gained traction in engineering applications. MCDA provides a structured approach to evaluating various alternatives based on multiple attributes, making it particularly suitable for industrial contexts where decisions must be made quickly, consistently, and transparently [11]. Among the spectrum of MCDA tools, the Weighted Sum Method (WSM) stands out for its simplicity, low computational effort, and ease of implementation [12]. In WSM, the final decision score is calculated as a linear combination of weighted performance scores across selected criteria, allowing for straightforward comparisons between competing adhesives.

Given the need for efficiency and clarity in the adhesive selection process, WSM is adopted in this study as the decision-support framework. Its intuitive formulation allows engineers and decision-makers to balance mechanical performance metrics obtained from experimental testing—especially those derived from modified Arcan tests—with practical considerations. This approach ensures that the selected adhesive not only meets mechanical and environmental demands but also integrates seamlessly into broader project goals.

In summary, this article bridges the gap between mechanical characterization and engineering decision-making. Through the use of advanced experimental methods like the modified Arcan test and a structured MCDA tool such as WSM, we propose a comprehensive framework for the robust selection of structural adhesives. This framework is designed to enhance reliability, reduce trial-and-error in product development, and facilitate the systematic integration of experimental insights into engineering practice.

2. Material and experimental methods

2.1. General information on the adhesives

The objective of this project is to identify and characterize a structural bonding solution suitable for applications in marine environments. Due to their favourable aging behavior under humid conditions, two types of two-component epoxy adhesives were proposed.

For confidentiality reasons, the commercial names of these adhesives cannot be disclosed. Therefore, the two adhesives will be referred to as Adhesive A and Adhesive B throughout this document. These adhesives were proposed by the industrial partner, and the purpose of the following sections is to evaluate them in order to identify the most suitable solution for the targeted application.

Adhesive A and Adhesive B are two-component epoxy paste adhesives already used in various industrial applications. According to the manufacturer, both adhesives demonstrate high shear strength, long-term durability, and resistance to moisture-induced aging—essential properties for marine environments. Both adhesives are supplied with 2 components (resin and hardener), and the mixing of each adhesive must strictly respect the ratios specified by the manufacturer and indicated in Tables 1 and 2.

According to Tables 1 and 2, for each of the two adhesives, the epoxy resin and its corresponding hardener must be mixed at room temperature in the ratio specified by the manufacturer. These components are mixed in 50 mL or 100 mL polypropylene containers, which limit adhesion. A laboratory balance, the Precise™ XT22A, ensures the accuracy of the mixing ratio.

Table 1. *Technical specifications for adhesive A*

Property	*Resin*	*Hardener*	*Mixture*
Color (visual)	Yellow	Blue	Dark green
Density	1.2	1.0	~1.1
Viscosity at 25 °C (Pa.s)	100-300	0.6-1.4	35-45
Pot life (100 g at 25 °C)	-	-	120-200 min
Shear strength at 23 °C	-	-	>30 MPa
Mixing ratio (by weight)	100	40	-
Mixing ratio (by volume)	100	50	-

THE ANNALS OF "DUNAREA DE JOS" UNIVERSITY OF GALATI
FASCICLE IX. METALLURGY AND MATERIALS SCIENCE
N°. 2 - 2025, ISSN 2668-4748; e-ISSN 2668-4756
Article DOI: https://doi.org/10.35219/mms.2025.2.05

Table 2. *Technical specifications for adhesive B*

Property	*Resin*	*Hardener*	*Mixture*
Color (visual)	Gray	Beige	Gray
Density	1.4	0.9	~1.2
Viscosity at 25 °C (Pa.s)	380-720	Thixotropic	Thixotropic
Pot life (100 g at 25 °C)	-	-	80-90 min
Shear strength at 23 °C	-	-	>17 MPa
Mixing ratio (by weight)	100	60	-
Mixing ratio (by volume)	100	100	-

Previous experiments [10, 13] have shown that optimal homogeneity is achieved using a Speedmixer™ DAC 150.1 FVZ. This specialized device mixes for 0 to 5 minutes at speeds ranging from 300 to 3500 rpm. For both adhesives, a speed of 2500 rpm was used for 4 minutes. These parameters ensure the desired homogeneity without overheating the mixture.

Finally, the mixture can be used within the pot life specified by the manufacturer (Tables 1 and 2) to bond surfaces that have been pre-prepared (e.g. by cleaning and mechanical polishing). The assembled joints are then subjected to the recommended polymerization cycles.

For epoxy adhesives, the choice of the polymerization cycle significantly affects the resulting mechanical properties. According to the manufacturer, shear strength may vary depending on the temperature and duration of the curing cycle.

The polymerization cycles used in this study were defined by the industrial partner based on the specifics of the intended application, and are listed in Table 3. These conditions are strictly followed throughout the fabrication of all bonded assemblies.

The experimental setup used to carry out these polymerization cycles is a Memmert UF 110 climate chamber, which provides a temperature range from 20 °C to 310 °C.

Table 3. *Polymerization Cycles*

Adhesive	*Temperature*	*Duration*
A	50 °C	12 hours
B	23 °C	7 days

2.2. Sample Preparation

In order to study the mechanical behavior of adhesives, modified Arcan tests were performed. Several previous studies [6, 14-16] have highlighted the relevance of these tests for the mechanical characterization of bonded joints. This test campaign provides a basis for comparing the mechanical performance of the two proposed adhesives, independent of the substrates used. In this section, we present the experimental protocol and the results of these tests.

The geometry of the samples used is shown in Figure 1. Various researchers have demonstrated that this geometry yields good repeatability under different loading types and conditions [10, 13-14, 17-18].

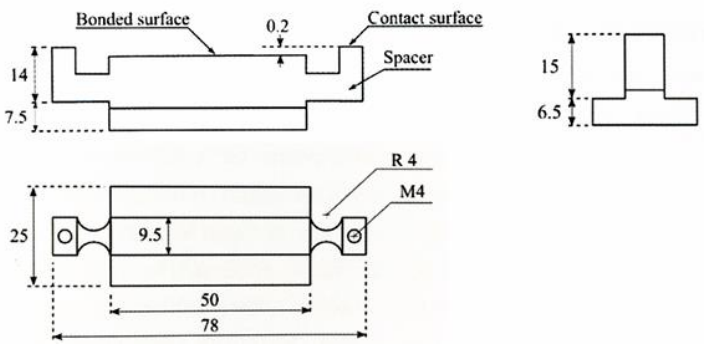

Fig. 1. *Main dimensions of the geometry (not to scale)* [19]

THE ANNALS OF "DUNAREA DE JOS" UNIVERSITY OF GALATI
FASCICLE IX. METALLURGY AND MATERIALS SCIENCE
Nº. 2 - 2025, ISSN 2668-4748; e-ISSN 2668-4756
Article DOI: https://doi.org/10.35219/mms.2025.2.05

A key feature of the Arcan specimen is the presence of "beaks" (Fig. 2) that minimize edge effects during the test. These features reduce stress concentrations at the adhesive joint edges, allowing characterization without premature crack initiation. Additionally, the loading condition promotes cohesive failure (within the adhesive) rather than adhesive failure (at the interface with the substrates).

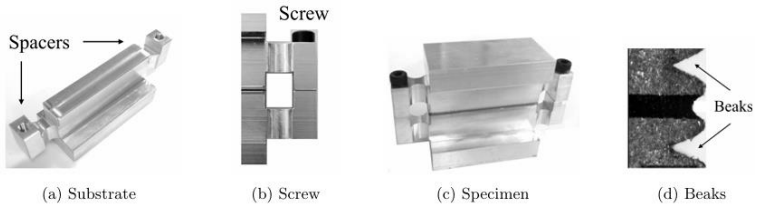

Fig. 2. *Modified Arcan specimen* [10]

An Arcan specimen is assembled by bonding two substrates as shown in Figure 2. The bonding procedure begins with surface preparation: fine polishing using abrasive paper (grade #180) to ensure optimum adhesion (Fig. 3.a). The adhesive is then applied to the two substrates (Fig. 3.b), which are aligned and held in place by screws through spacers (Fig. 3.c). The spacers align the substrates and maintain this position during bonding. Their thickness also controls the thickness of the adhesive layer (typically 0.4 mm). For reasons of reproducibility, screws are tightened to 1.5 N-m using a torque screwdriver. After assembly, the polymerization cycle specific to each adhesive (Table 3) is applied.

Finally, spacers are removed and the specimen is ready for testing. A speckle pattern (Fig. 3.d) may be applied for Digital Image Correlation (DIC), which is explained further in this section.

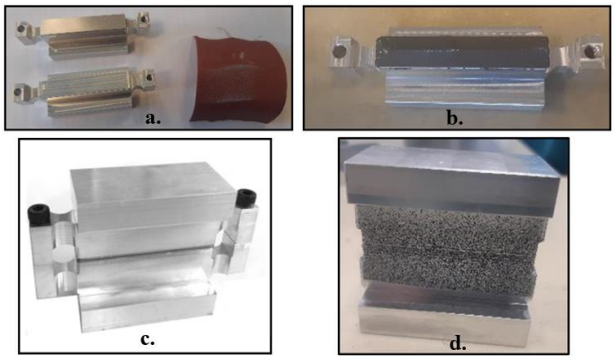

Fig. 3. *Sample preparation: a - surface polishing; b - adhesive application; c - assembled sample; d - sample ready for testing*

2.3. Substrates

The substrates are made of aluminium alloy AW2017, chosen for its ease of machining and resistance to harsh environmental conditions. Some of its mechanical properties are shown in Table 5.

Table 5. *Mechanical Properties of AW2017 Aluminium Alloy*

Properties	*Value*	*Unit*
Density	8	$g.cm^{-3}$
Thermal conductivity	130-200	$W.mK^{-1}$
Young's modulus	75	*GPa*
Shear modulus	27.2	*GPa*
Tensile strength	250-370	*MPA*

2.4. Experimental Setup

The test setup is shown in Figure 4 and includes:

• The INSTRON 1342 tensile testing machine (Fig. 4.a);

• The modified Arcan fixture (Figure 7);

• The GOM 5M Digital Image Correlation (DIC) system (Figures 4.b, 4.c)

The INSTRON machine uses hydraulic actuation. Main specifications are shown in Table 6.

Table 6. *INSTRON 1342 specifications*

Specifications	*Value*	*Unit*
Max force	+/-100	*kN*
Max speed	10	*mm/s*

THE ANNALS OF "DUNAREA DE JOS" UNIVERSITY OF GALATI
FASCICLE IX. METALLURGY AND MATERIALS SCIENCE
Nº. 2 - 2025, ISSN 2668-4748; e-ISSN 2668-4756
Article DOI: https://doi.org/10.35219/mms.2025.2.05

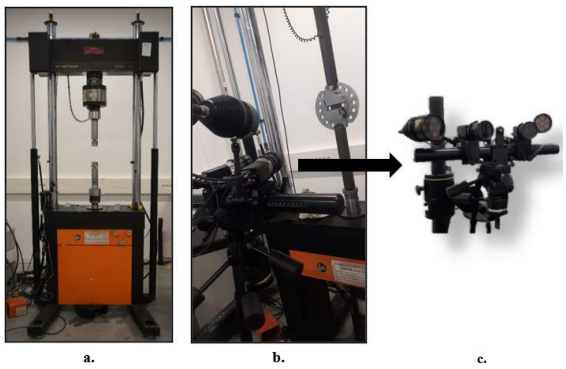

Fig. 4. *Experimental set-up for Arcan tests: a - INSTRON 1342; b - Arcan set-up during test; c - GOM 5M*

The modified Arcan fixture allows combined loading conditions (tension, shear, or mixed tension-shear). By rotating the fixture by an angle θ relative to the machine's axis, the loading type can be easily changed. Figure 5. shows the three applied loading types.

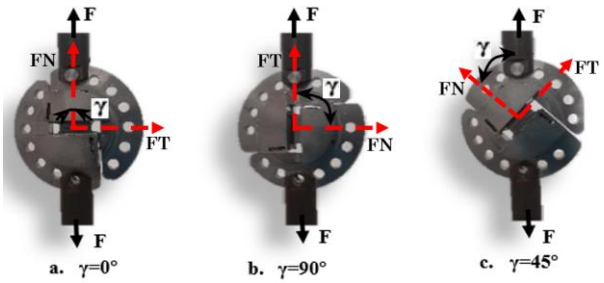

Fig. 5. *Different loads applied with the Arcan device: a - tensile; b - shear; c - tensile-shear*

Digital image stereo-correlation (DIC) is the preferred method of test analysis, particularly in the field of research, because of its ability to accurately follow sample displacements and deformations during testing. The special feature of DIC is access to the distribution of kinematic fields, such as displacements and even deformations, enabling out-of-plane displacements to be determined. Further details can be found in the literature [20].

The GOM 5M digital image stereo-correlation system, shown in Figure 4.c, consists of two cameras which record images during the test at a set frequency. The advantage of using DIC is that it can also detect motion in a third direction (out-of-plane), making it independent of the relative positron variation between sample and system.

DIC is used to determine the displacement fields and, by derivation, the deformation of the sample. The principle of this method is based on the tracking of a pattern identified in the reference image for all so-called deformed images. The set of recorded images forms a film, from which we extract a measurement. Random coding is achieved using two spray paints (white and black). First of all, a white background is created, onto which black spots with dimensions ranging from 100 µm to 1000 µm are applied (Fig. 6).

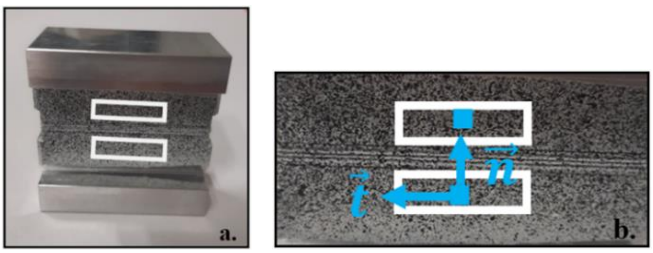

Fig. 6. *A sample coded with a random pattern: a - area of interest; b - normal and tangential directional vectors*

THE ANNALS OF "DUNAREA DE JOS" UNIVERSITY OF GALATI
FASCICLE IX. METALLURGY AND MATERIALS SCIENCE
No. 2 - 2025, ISSN 2668-4748; e-ISSN 2668-4756
Article DOI: https://doi.org/10.35219/mms.2025.2.05

Finally, the recorded test data (images and associated forces) with the digital image stereo-correlation system are analysed using ARAMIS v6.3.1 software. In the case of the Arcan sample, the area of interest to be analysed is chosen in the central part of the substrate, close to the adhesive joint (Fig. 6). More precisely, displacement fields are measured in the normal and tangential directions between these two zones of interest, as illustrated in Figure 6.b.

These experimental tools for modified Arcan device enable robust experimental characterization of the adhesive joint, leading to reliable results through judicious exploitation of these displacement or deformation fields.

3. Results

3.1. Experimental test results

Fig. 7 presents the results from the main Arcan tests performed. These are all monotonic tests conducted under force control, with a loading rate of 0.2 kN/s. Displacement fields measured via DIC allows us the reconstruction of force–displacement curves, where the displacement represents the relative movement between the two bonded substrates.

Here, the x-axis of the graphs in Figure 7 represents the relative displacement (normal or tangential) between two points on the substrates located 1.5 mm from the mid-plane of the adhesive joint (Fig. 6). The y-axis represents the corresponding force measured in the same direction by the load cell.

As discussed earlier, loading configurations include:

- Tension (Figure 7.a);
- Shear (Figure 7.b);
- Combined tension-shear at 45° (Figures 7.c and 7.d show normal and tangential force-displacement curves respectively).

These initial mechanical tests allow us comparison of the two adhesives — A and B. Three tests were conducted for each loading type, and good repeatability was observed for both adhesives.

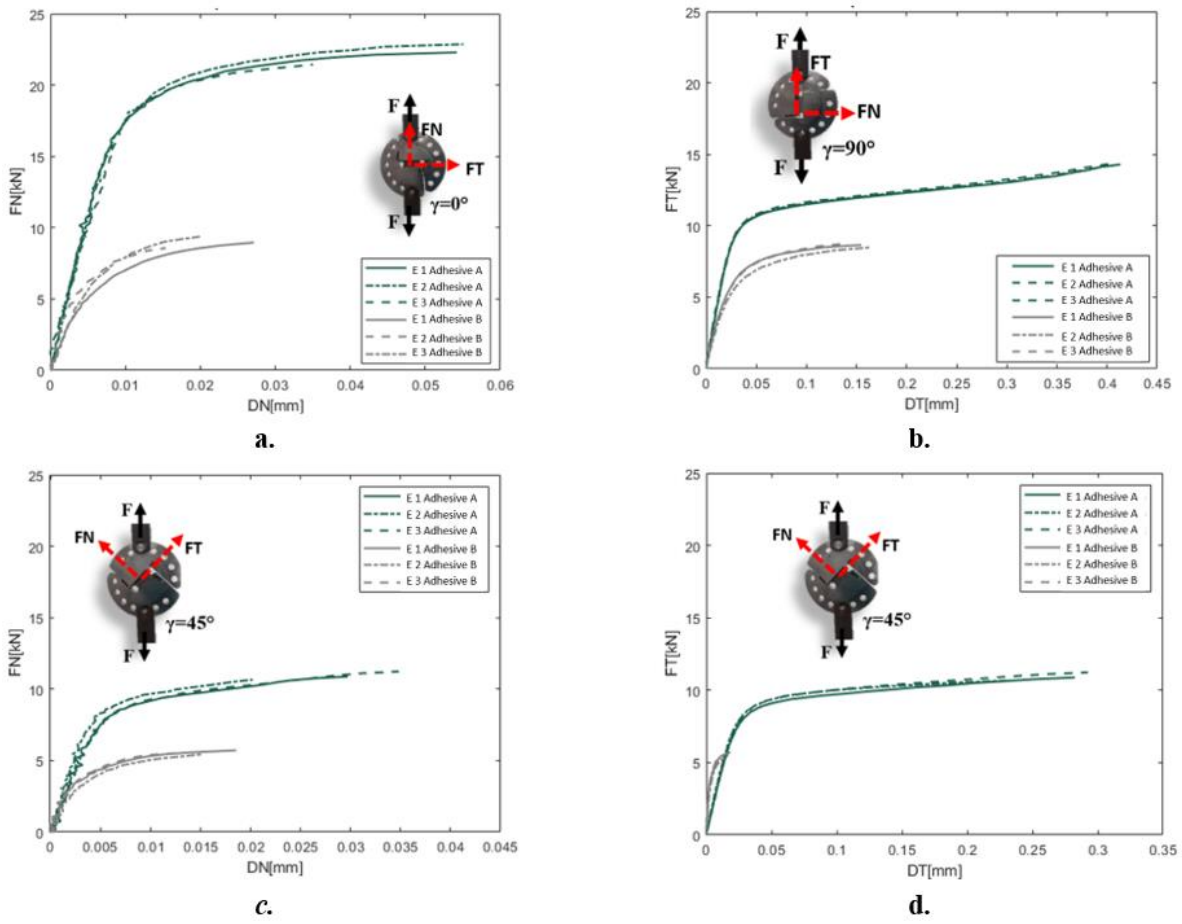

Fig. 7. *Adhesive behavior: a - tensile; b - shear; c - tension-shear (FN); d - tension-shear (FT)*

THE ANNALS OF "DUNAREA DE JOS" UNIVERSITY OF GALATI
FASCICLE IX. METALLURGY AND MATERIALS SCIENCE
No. 2 - 2025, ISSN 2668-4748; e-ISSN 2668-4756
Article DOI: https://doi.org/10.35219/mms.2025.2.05

Preliminary analysis of these curves reveals that the mechanical properties of adhesive A (e.g., apparent yield limit and ultimate force) are significantly higher than those of adhesive B, across all three loading types (tension, shear, and combined tension-shear).

Figure 8 summarizes the ultimate loads obtained for both adhesives under different loadings. In each case, the variation in maximum force between tests is less than 5% of the average value. This figure clearly highlights the performance gap between the two adhesives.

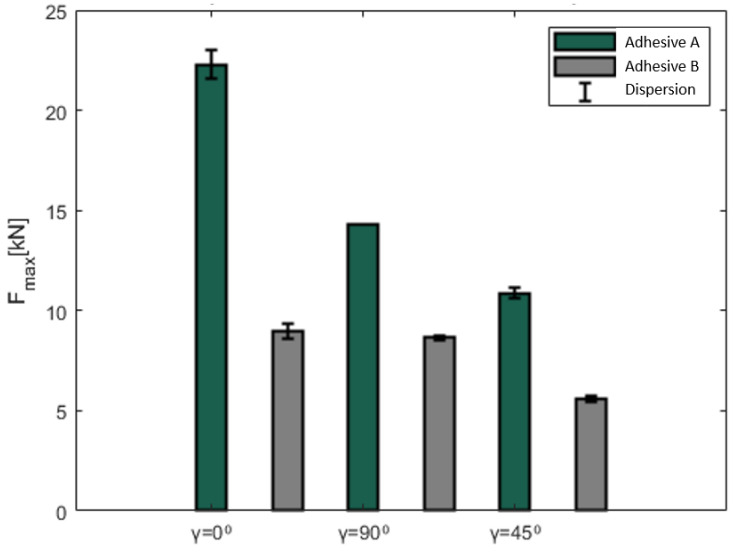

Fig. 8. *Dispersion in fracture behavior*

Figures 9 and 10 show the envelopes of the yield stresses and breaking loads, respectively, for the two adhesives. These curves are plotted in the tension-shear plane, and strains are estimated by dividing the force by the bonded area. However, due to the non-uniform stress distribution in the modified Arcan sample, the average normal and shear strain are corrected using the following equations [8]:

$$\sigma_{max\ \_el} = 1.12\sigma_{moy}, avec\ : \sigma_{moy} = \frac{FN}{S_c} \quad (1)$$

$$\tau_{max\ \_el} = 1.29\tau_{moy}, avec : \tau_{moy} = \frac{FT}{S_c} \quad (2)$$

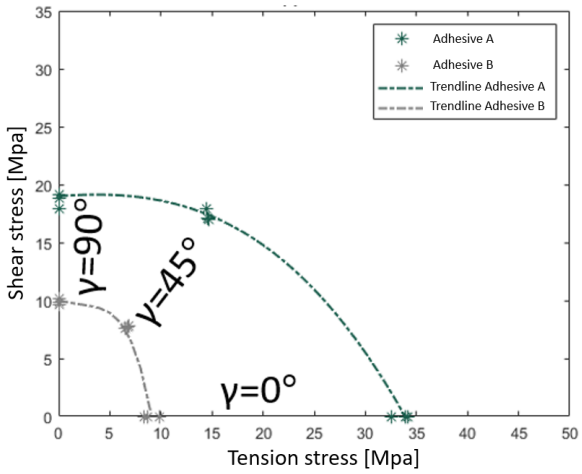

Fig. 9. *Elasticity envelopes*

THE ANNALS OF "DUNAREA DE JOS" UNIVERSITY OF GALATI
FASCICLE IX. METALLURGY AND MATERIALS SCIENCE
N°. 2 - 2025, ISSN 2668-4748; e-ISSN 2668-4756
Article DOI: https://doi.org/10.35219/mms.2025.2.05

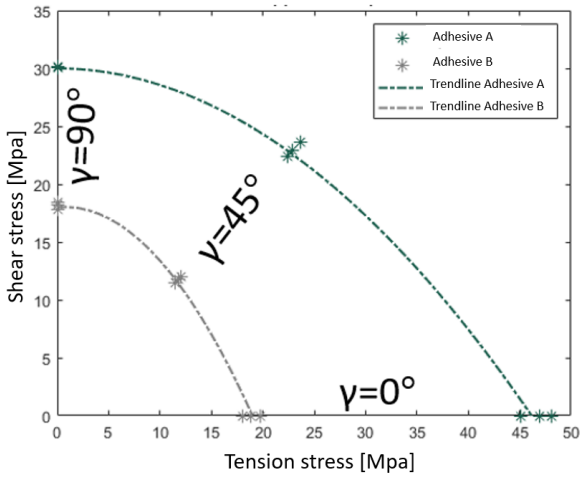

Fig. 10. *Failure envelopes*

These corrected stress estimates are consistent with values obtained through inverse identification techniques that model the test using finite element methods [8, 21].

Lastly, modified Arcan tests also provide insights through visual analysis of the fracture surfaces. Fracture patterns for samples bonded with adhesive B (Figures 11.A, 11.B, 11.C) suggest better adhesion to aluminium substrates compared to those bonded with adhesive A (Figures 11.D, 11.E, 11.F). In particular, joints bonded with adhesive B generally fail cohesively (within the adhesive), whereas joints bonded with adhesive A tend to show cohesive failure in tension (Figure 11.F) and mixed cohesive/adhesive failure under shear or combined load (Figures 11.D, 11.E).

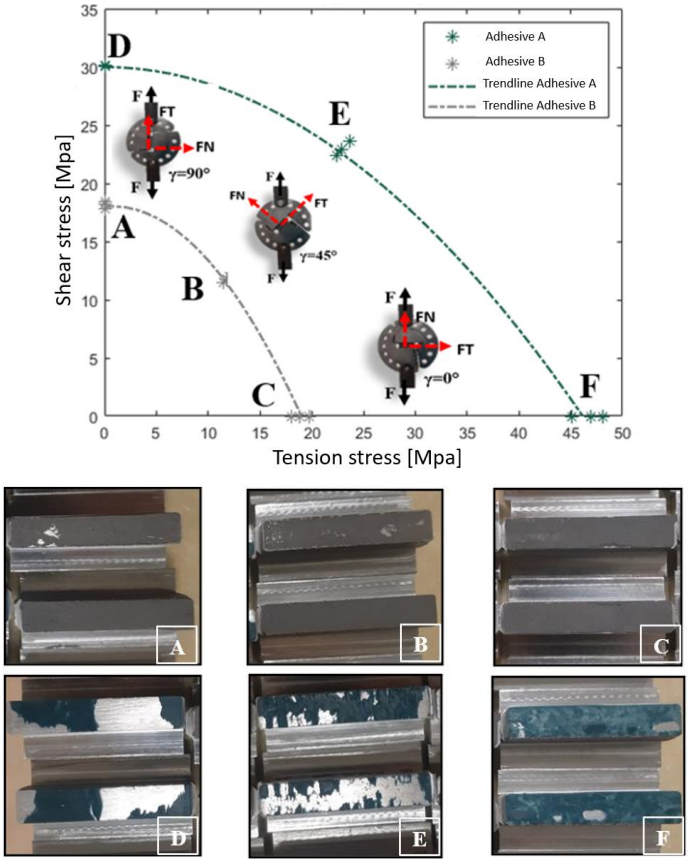

Fig. 11. *Failure modes for each load type*

THE ANNALS OF "DUNAREA DE JOS" UNIVERSITY OF GALATI
FASCICLE IX. METALLURGY AND MATERIALS SCIENCE
N°. 2 - 2025, ISSN 2668-4748; e-ISSN 2668-4756
Article DOI: https://doi.org/10.35219/mms.2025.2.05

These experimental tests enabled us to identify the maximum force and the maximum strain at rupture under the assumption of complete plastic deformation. For the first part, we identified the elastic modulus. These parameters enabled us to compare the two adhesives in terms of mechanical behavior.

3.2. Selection of the Structural Adhesive

The work presented above, along with the results obtained, is intended to lead to an objective selection of the adhesive to be used in future analyses and applications. In order to choose the most appropriate adhesive, selection criteria must be defined in alignment with the project specifications.

The chosen criteria can be grouped and assessed using Multi-Criteria Decision Analysis (MCDA) methods. These methods are especially useful in industrial contexts due to their simplicity and ease of implementation. Numerous types of MCDA methods are documented in the literature. For example, Goh [22] provides a review of several widely used decision methods, evaluating their advantages and disadvantages — such as ease of implementation, required effort, and need for additional tools.

Figure 12 lists the main decision analysis methods cited in the literature, along with how frequently they appear in reported studies.

Given the need for a quick and simple analysis in this study, the Weighted Sum Method (WSM) was selected for choosing the optimal adhesive. WSM is an elementary MCDA method where the final value of a given solution is calculated as the sum of the weights of its evaluation against each criterion [22]. For more details, the mathematical principle of the process is described in [23].

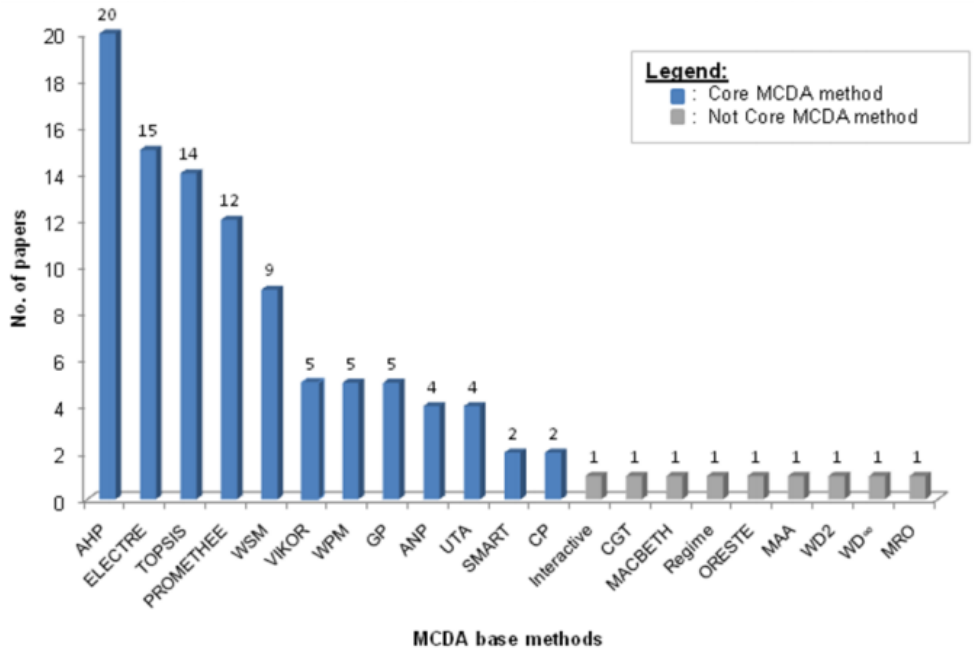

Fig. 12. *The main decision analysis methods presented in the publications* [22]

The calculation procedure for adhesive selection by weighted sum is shown in Tables 7, 8 and 9. In particular, the method involves first establishing a weighting for each selected criterion (Table 7). On the basis of this weighting, the importance of the criterion given by scores from 0 (not important) to 3 (very important) was established. Secondly, the criteria are ranked by scores from 0 to 10 with the meaning explained in Table 8. According to this notation, a score closer to 0 means that the adhesive is not suitable under the given conditions, and a score closer to 10 indicates suitable properties. The final step in this method is the effective sum of these scores for each adhesive (Table 9). The scores given for each criterion are multiplied by their weight. The resultant product is added together to form a weighted sum representing the benchmark to be compared. The adhesive with the highest score is classified as optimal. Scores are given according to the results obtained from the experimental tests (modified Arcan).

Therefore, based on the scores obtained using this method, adhesive A is identified as the optimal adhesive for the considered application.

THE ANNALS OF "DUNAREA DE JOS" UNIVERSITY OF GALATI
FASCICLE IX. METALLURGY AND MATERIALS SCIENCE
N°. 2 - 2025, ISSN 2668-4748; e-ISSN 2668-4756
Article DOI: https://doi.org/10.35219/mms.2025.2.05

Table 7. *Evaluation Weights*

Weight	*Meaning*
0	Not important
1	Slightly important
2	Important
3	Very important

Table 8. *Selection Criteria*

Criterion	*Min Score*	*Meaning*		*Max Score*	*Meaning*	
σ_{max} (strength)	0	0 MPa	No strength	10	40 MPa	Very high strength
$D_{\sigma_{max}}$ (Reproducibility)	0	>40% variation	Poor	10	<5% variation	Very good
N_f (Failure Mode)	0	Adhesive failure		10	Cohesive failure	

Table 9. *Weighted Sum Calculation*

Test Type	*Arcan*						*Total Weighted Score*
Criteria	σ_{max}		N_f		$D_{\sigma_{max}}$		
Weights	3		2		2		
Adhesive A	8	**24**	6	**12**	8	**16**	52
Adhesive B	4	**12**	9	**18**	7	**14**	44

4. Conclusions and perspectives

This study proposes a robust and scalable framework for selecting structural adhesives using a combination of experimental testing and the Weighted Sum Method for decision-making. The methodology was applied to two epoxy adhesives, evaluated through modified Arcan tests under tensile, shear, and mixed loading configurations. These tests provided a clear mechanical comparison of the adhesives, enabling their classification based on performance indicators such as strength, failure mode, and repeatability.

The novelty and strength of this approach lie in its flexibility and industrial relevance. By using WSM, the selection process becomes transparent and reproducible, enabling engineers to define weighted criteria that reflect the specific needs of an application. Although this study relied on a single type of mechanical test (modified Arcan), the methodology allows for the integration of additional tests—both on bulk adhesive properties (e.g., tensile, shear) and various joint configurations (e.g., TAST, butt-joint, etc.).

This strategy is particularly beneficial in industrial environments where adhesive performance must align with specific service conditions (e.g., temperature, humidity, dynamic loads). The method ensures that the test data used are representative of the application scenario and encourages execution under conditions close to real-world operation.

However, the proposed framework also has some limitations. We mention here the cost and duration of the experiments since performing the relevant mechanical tests, in particular on bonded joints, is resource intensive. Finally, subjectivity in scoring is also a limitation of the method. WSM relies on subjective scores assigned to each criterion, and if not carefully controlled, this could introduce bias into the decision.

In order to improve these aspects, two suggestions can be offered as a starting point for future work:

- Numerical simulation as a substitute or complement to experimental testing - If the mechanical behavior of adhesives and substrates is already known, simulations can reproduce the operating conditions and reduce the dependence on experimental testing.

- Minimize subjectivity - Ideally, scoring should be performed by multiple evaluators and the average score should be used in the WSM calculation. This collaborative assessment can reduce individual bias and improve the reliability of decisions.

In conclusion, this work demonstrates the utility of the WSM method in adhesive selection and encourages its broader use across various industrial contexts. The proposed method offers a systematic path from experimental mechanics to informed engineering decisions and can be adapted to a wide range of structural applications.

References

[1]. da Silva L. F. M., *et al.*, *2 Handbook of Adhesion Technology*, 2nd ed., Springer Heidelberg, 2018.
[2]. da Silva S. L. M., *et al.*, *Quasi-Static Constitutive and Strength Tests, Testing Adhesive Joints*, Weinheim: Wiley-VCH, p. 79-162, 2012.
[3]. Chen Z., *et al.*, *Fracture Toughness of Bulk Adhesives in Mode I and Mode III and Curing Effect*, International Journal of Fracture, 167(2), p. 221-34, https://doi.org/10.1007/s10704-010-9547-9, 2011.
[4]. Ilioni A., *et al.*, *A Viscoelastic-Viscoplastic Model to Describe Creep and Strain Rate Effects on the Mechanical Behaviour of Adhesively-Bonded Assemblies*, International Journal of Adhesion and Adhesives, 82, p. 184-95, 10.1016/j.ijadhadh.2017.12.003, 2018.
[5]. Cognard J. Y., *et al.*, *Development of an Improved Adhesive Test Method for Composite Assembly Design*, Composites Science and Technology, 65, p. 359-68, DOI: 10.1016/j.compscitech.2004.09.008, 2005.
[6]. Cognard J. Y., *et al.*, *Analysis of the Nonlinear Behavior of Adhesives in Bonded Assemblies-Comparison of TAST and Arcan Tests*, International Journal of Adhesion and Adhesives, 28(8), p. 393-404, https://doi.org/10.1016/j.ijadhadh.2008.04.006, 2008.
[7]. Papanicolaou G. C., *et al.*, *Experimental and Numerical Investigation of Balanced Boron/Epoxy Single Lap Joints Subjected to Salt Spray Aging*, International Journal of Adhesion and Adhesives, 68, p. 9-18, DOI: 10.1016/j.ijadhadh.2016.01.009, 2016.
[8]. Badulescu C., *et al.*, *Analysis of the Low Temperature-Dependent Behaviour of a Ductile Adhesive under Monotonic Tensile/Compression-Shear Loads*, International Journal of Adhesion and Adhesives, 36, p. 56-64, DOI: 10.1016/j.ijadhadh.2012.03.009, 2012.
[9]. Thévenet D., *et al.*, *Experimental Analysis of the Behavior of Adhesively Bonded Joints under Tensile/Compression-Shear Cyclic Loadings*, International Journal of Adhesion and Adhesives, 44, p. 15-25, DOI: 10.1016/j.ijadhadh.2013.01.011, 2013.
[10]. Ilioni A., *Influence of Water Ageing on the Behaviour of Adhesives. A Rapid Characterization of the Evolution of Mechanical Properties of Bonded Joints*, https://theses.hal.science/tel-01744438v1/file/These-2017-SPI-Mecanique_des_solides_des_materiaux_des_structures_et_des_surfaces-ALIONI_Alin.pdf, 2017.
[11]. Goh W. A., *Applying Multi-Criteria Decision Analysis for Software Quality Assessment Methods*, p. 1-136, Mathematics 2010.
[12]. Maliene V., *et al.*, *Dispersion of relative importance values contributes to the ranking uncertainty: Sensitivity analysis of Multiple Criteria Decision-Making methods*, Applied Soft Computing Journal, 67, p. 286-298, DOI: 10.1016/j.asoc.2018.03.003, 2018.
[13]. Dumont V., *On the Durability of Structural Adhesive Bonds in Thermal Environments: Application to Space-Oriented Optical Systems*, https://theses.hal.science/tel-03349315v1/file/2020_vincent_dumont_these_locale.pdf, 2020.
[14]. Alfonso L., *et al.*, *Use of the Modified Arcan Fixture to Study the Strength of Bonded Assemblies for Automotive Applications*, International Journal of Adhesion and Adhesives, 80, p. 104-14, DOI: 10.1016/j.ijadhadh.2017.09.014, 2018.
[15]. Badulescu C., *et al.*, *Characterization and Modelling of the Viscous Behaviour of Adhesives Using the Modified Arcan Device*, Journal of Adhesion Science and Technology, 29(5), p. 443-61, DOI: 10.1080/01694243.2014.991483, 2015.
[16]. Stamoulis G., *et al.*, *Investigating the Fracture Behavior of Adhesively Bonded Metallic Joints Using the Arcan Fixture*, International Journal of Adhesion and Adhesives, 66, p. 147-59, DOI: 10.1016/j.ijadhadh.2016.01.001, 2016.
[17]. Arnaud N., *et al.*, *A Tension/Compression-Torsion Test Suited to Analyze the Mechanical Behaviour of Adhesives under Non-Proportional Loadings*, International Journal of Adhesion and Adhesives, 53, p. 3-14, DOI: 10.1016/j.ijadhadh.2014.01.013, 2014.
[18]. Cognard J. Y., *et al.*, *On Modelling the Behaviour of a Ductile Adhesive under Low Temperatures*, International Journal of Adhesion and Adhesives, 47, p. 46-56, DOI: 10.1016/j.ijadhadh.2013.09.024, 2013.
[19]. Alfonso Medina H. L., *Characterization and modeling of multi-material assemblies under mixed quasi-static loadings for the design of automotive structures*, https://theses.hal.science/tel-01453047v2/file/These-2016-EDSM-Genie_mecanique-ALFONSO_Hugo_Leonardo.pdf, 2016.
[20]. Kavdir E. Ç., *et al.*, *The Investigation of Mechanical Properties of a Structural Adhesive via Digital Image Correlation (DIC) Technic*, Composites Part B: Engineering, 173(May): 106995, DOI: 10.1016/j.compositesb.2019.106995, 2019.
[21]. Maurice J., *et al.*, *Characterization and Modelling of the 3D Elastic-Plastic Behaviour of an Adhesively Bonded Joint under Monotonic Tension/Compression-Shear Loads: Influence of Three Cure Cycles*, Journal of Adhesion Science and Technology, 27(2), p. 165-81, DOI: 10.1080/01694243.2012.701528, 2013.
[22]. Goh W. A., *Applying Multi-Criteria Decision Analysis for Software Quality Assessment Methods*, p. 1-136, FULLTEXT01.pdf, 2010.
[23]. Maliene V., *et al.*, *Dispersion of relative importance values contributes to the ranking uncertainty: Sensitivity analysis of Multiple Criteria Decision-Making methods*, Applied Soft Computing Journal, 67, p. 286-298, DOI: 10.1016/j.asoc.2018.03.003, 2018.

THE ANNALS OF "DUNAREA DE JOS" UNIVERSITY OF GALATI
FASCICLE IX. METALLURGY AND MATERIALS SCIENCE
No. 2 - 2025, ISSN 2668-4748; e-ISSN 2668-4756
Article DOI: https://doi.org/10.35219/mms.2025.2.06

STUDIES AND RESEARCH ON GLASS THERMOFORMING

Beatrice Daniela TUDOR
"Dunarea de Jos" Unniversity of Galati, Romania
e-mail: beatrice.tudor@ugal.ro

ABSTRACT

The paper presents a study on the properties that can influence the glass thermoforming process, and an experimental research on glass plate samples, with the aim of observing how glass deforms through thermoforming, using concave and convex support shapes and exposure to temperature, in different areas inside the oven.

KEYWORDS: glass, thermoforming, viscosity

1. Introduction

Glass is one of the oldest materials used by man. Having become an indispensable material in human life, glass is currently produced in large quantities. In general, thermoforming is the technique of obtaining a piece from a thermo formable material, using heat to make it take the desired configuration, using for this purpose a form appropriates to the intended purpose.

Thermoforming is the name of the operation of hot forming glass, which is generally flat. The process consists of placing glass sheets, in a certain position, with or without a support, in an oven.

Thermoforming consists of shaping a piece of glass, solid and flat, placed on a support, usually around its perimeter, in an oven, initially cold, and heating it until it becomes viscous. Near temperatures of 700 °C, under the action of weight, the plate deforms and stretches until the desired shape is obtained, in contact with the walls of the model. The piece can also be shaped by blowing. suction, or by some mechanical action [2, 4, 8].

Thermoforming steps: The steps of thermoforming glass are shown in Figure 1.

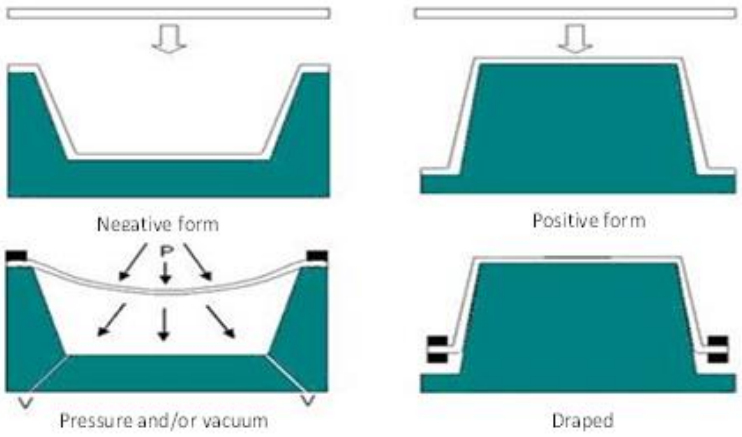

Fig. 1. *Stages of glass thermoforming*

In addition to creating artistic pieces, this process is used industrially, in the case of flat glass, in the manufacture of windshields and other components for motor vehicles, lenses, television screens, and glass containers.

The main difficulty lies in achieving uniform thickness of the formed piece, which can lead to additional costs. Artisans, in turn, face the same difficulties in obtaining the desired configuration when shaping glass by thermoforming.

THE ANNALS OF "DUNAREA DE JOS" UNIVERSITY OF GALATI
FASCICLE IX. METALLURGY AND MATERIALS SCIENCE
No. 2 - 2025, ISSN 2668-4748; e-ISSN 2668-4756
Article DOI: https://doi.org/10.35219/mms.2025.2.06

In the case of large-scale production by thermoforming, a correction/improvement process can be easily developed industrially to remedy deficiencies and obtain the desired object. However, for artisanal or one-off manufacturing, it is difficult to apply without wasting money and time.

Thermal regime: Thermoforming is, in practice, a heating process, using, to obtain the desired effect, refractory moulds so as to give the piece a certain, particular, desired, imagined configuration (most often, concave). The glass, under the effect of heat, softens, "sinks" (sags) and faithfully copies the configuration of the form.

The shaping of the glass is determined by its viscosity, which is temperature-dependent.

The glass, placed above the mould, is heated to a high temperature (approximately 800 °C). The temperature is increased progressively, with the glass taking, under the action of gravity, the configuration of the 3D relief of the mould.

The thermal regime of the furnace, can be broken down into four basic stages (Figure 2).

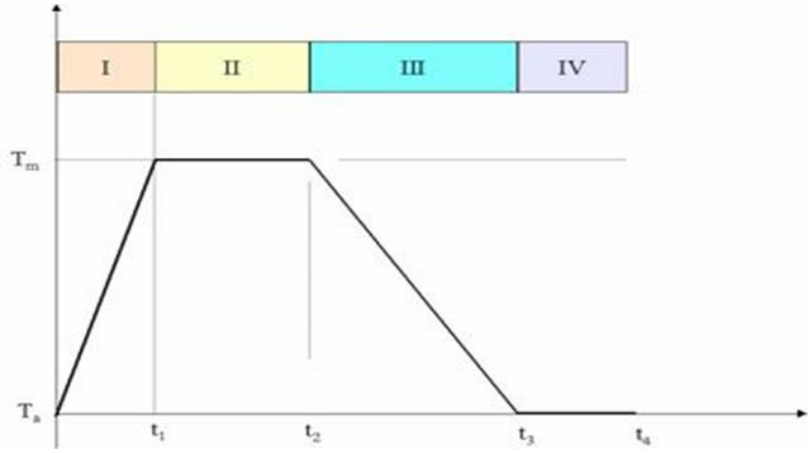

Fig. 2. *Thermal regime during thermoforming*

Heating: The glass sheet (S), placed on the mould (M) (Figure 3), inside the oven, initially at ambient temperature, is heated in stages.

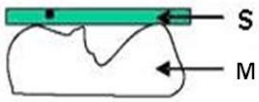

Fig. 3. *The mold-glass plate assembly used in thermoforming*

The purpose of heating is to quickly obtain a well-defined temperature, as homogeneous as possible in the surface plane and in the thickness of the plate. It is advisable to ensure a temperature increase on the platforms so as to completely avoid the risk of thermal cracking.

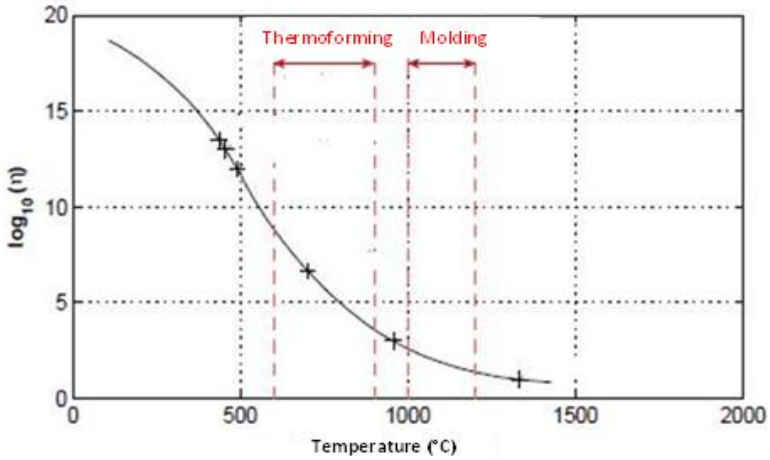

Fig. 4. *Variation of glass viscosity with temperature*

THE ANNALS OF "DUNAREA DE JOS" UNIVERSITY OF GALATI
FASCICLE IX. METALLURGY AND MATERIALS SCIENCE
No. 2 - 2025, ISSN 2668-4748; e-ISSN 2668-4756
Article DOI: https://doi.org/10.35219/mms.2025.2.06

There are three possible methods:

- by contact with a heating body, a method based on thermal conductivity: the main disadvantage is that it induces a very high temperature heterogeneity across the thickness of the glass plate;
- by convection, which leads to good temperature homogeneity across the thickness of the glass plate, but has the disadvantage of a long process duration.
-by radiation, the most common method which has the advantage of rapid heating but which can induce a certain heterogeneity across the thickness of the glass plate when it is thicker [1, 3].

Forming stage: Temperature is kept constant inside the oven, to allow the glass to soften. Under the action of weight, the plate deforms, and stretches/adheres until it covers the mould, faithfully reproducing its deformations, in contact with the soft glass plate (Figure 5).

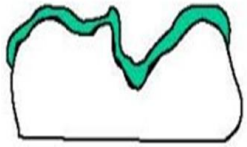

Fig. 5. *Thermoformed part, at the end of the heating process*

Cooling stage: Cooling is carried out in the third stage, and is characterized by controlled cooling, at ambient temperature, which allows the glass to resolidify, while preserving the configuration of the part, obtained at the moment of part-shell contact, and avoiding the appearance of significant residual stresses [5].

Separation of the profiled part: This separation takes place at ambient temperature, and represents the last step of the thermoforming process (Figure 6).

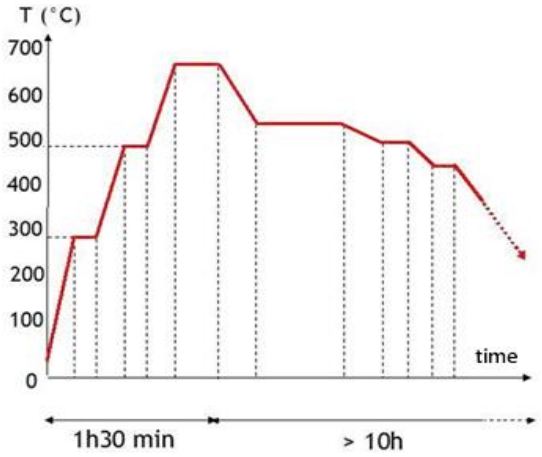

Fig. 6. *Diagram of the glass thermoforming cycle*

The heating process is divided into three main stages:

- heating to a temperature of approximately 700 °C;
- processing or forming stage: the minimum temperature reached corresponds to the softening point at which the glass deforms under the action of its own weight in a visible way; at this temperature, a stage long enough to allow the piece to take the configuration of the shape under the effect of gravity is carried out;
- cooling: the glass piece is cooled to ambient temperature; this cycle is carried out slowly (approximately 10 hours) so as not to damage the piece produced under the effect of too rapid cooling.

As a result of this process, the flat shape of the glass acquires a different configuration, a new relief or a new texture. The softening of the glass, under the action of heat, allows the glass sheet to stretch, practically bend under its own weight, and take the configuration of a support form or a support material. The thickness of the glass determines the heating time and the fineness of the texture [6, 7].

The shaping depends on the imposed thermal regime, the geometry of the part and its properties. In the case of thermoforming, the most important characteristic of glass is viscosity. It is the one that controls the deformation rate, and it is dependent on temperature.

2. Experimental research on the glass thermoforming process

For the study of thermoforming, 2 moulds with a simple configuration were used, namely, two semi-cylinders with a diameter of 50 mm and a length of 60 mm. (Figure 7).

When thermoforming the concave glass plate, it was chosen to fix the plate to the edges of the mould,

THE ANNALS OF "DUNAREA DE JOS" UNIVERSITY OF GALATI
FASCICLE IX. METALLURGY AND MATERIALS SCIENCE
N°. 2 - 2025, ISSN 2668-4748; e-ISSN 2668-4756
Article DOI: https://doi.org/10.35219/mms.2025.2.06

and not to support it, in order to observe how the glass deforms, and how the thickness of the glass varies, during thermoforming, in free fall, in a cavity.

In the case of the convex shape, a glass plate was used, with a length equal to the unfolded length of the outer surface of the shape, and a width equal to that of the shape.

To avoid the glass sticking to the shape, and its subsequent breakage, a ceramic separator was used, mandatory, especially at thermoforming temperatures.

Figure 8 shows the two samples, prepared for insertion into the oven.

The samples were obtained in a silica bar furnace, from the faculty laboratories, based on an adopted cycle for thermoforming the two glass plates.

The obtained samples are presented in Figure 9.

Fig. 7. *Shapes used in the study of thermoforming: a-concave; b-convex*

Fig. 8. *Glass samples prepared for thermoforming*

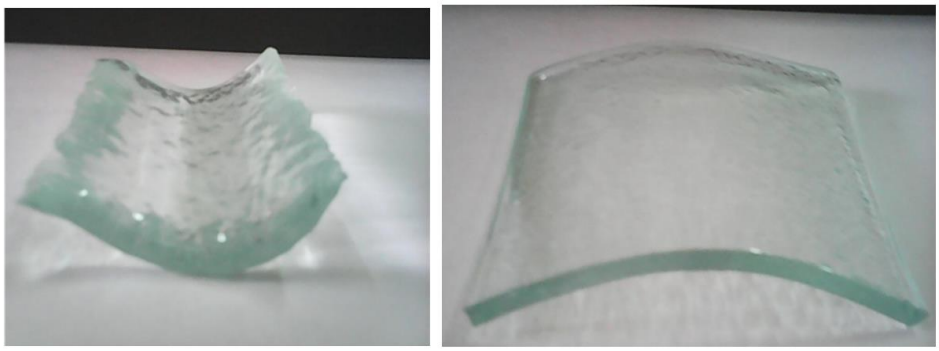

Fig. 9. *Thermoforming glass samples: a-concave; b-convex*

It is observed that the glass sample obtained on the concave mould took the configuration of its shape. The size of the glass was adapted to the mould opening, and not to its full length, which did not ensure complete coverage of the mould.

We found that the thickness of the glass plate did not change significantly, and the softening did not lead to a symmetrical "covering" of the metal mould.

It can be seen that in one of the areas, the glass sheet remained fixed to the edge of one of the mould walls, taking on a concave shape and reproducing its shape in its entirety, while reproducing less so that of the shape of the second wall (Figure 10).

THE ANNALS OF "DUNAREA DE JOS" UNIVERSITY OF GALATI
FASCICLE IX. METALLURGY AND MATERIALS SCIENCE
No. 2 - 2025, ISSN 2668-4748; e-ISSN 2668-4756
Article DOI: https://doi.org/10.35219/mms.2025.2.06

a. b. c.

Fig. 10. *Thermoformed, concave glass piece: a-side-top view; b-top view; c-texture of the sample*

On the opposite side, the edge of the glass piece descended onto the mould wall, acquiring a rounded shape, but the lack of material did not allow its full reproduction. The sample retained its thickness (Figure 10a), and the inner surface remained smooth and glossy (Figure 10b).

The outer surface of the sample acquired the texture of the ceramic separator (Figure 10c).

With glass samples cast on convex supports, two issues were encountered.

a. b.

Fig. 11. *Thermoformed part on convex mould: a-front view; b-top view*

In the case of samples (Figure 11.), maintained at the thermoforming temperature for a short period of time, the glass sample did not take the shape of the mould, but acquired only a small, non-uniform curvature along its length. It can be seen from Figure 12 that the sample was in the furnace within its loading zone, where the temperature is lower than in the area where the thermocouple is mounted.

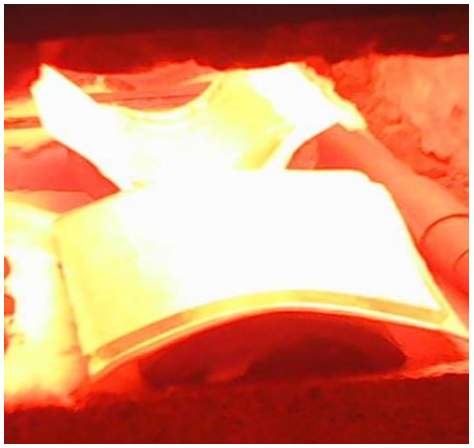

Fig. 12. *The furnace chamber, with the samples inside*

THE ANNALS OF "DUNAREA DE JOS" UNIVERSITY OF GALATI
FASCICLE IX. METALLURGY AND MATERIALS SCIENCE
No. 2 - 2025, ISSN 2668-4748; e-ISSN 2668-4756
Article DOI: https://doi.org/10.35219/mms.2025.2.06

In the case of the sample maintained for a longer period at the working temperature, a convex piece was obtained, cast on the same model.

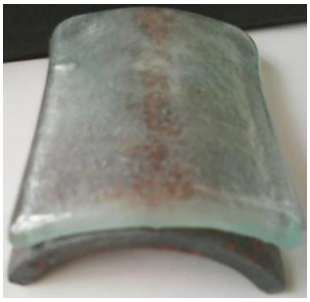

Fig. 13. *Second sample of convex shape*

The surface quality and edge shape of the sample are approximately the same as those of the concave sample. The edges have the same shape on both sides, determined by the softening of the glass, and its shaping, under the effect of its own weight on the mould.

The outer surface remained smooth and glossy, while the texture of the ceramic support used to avoid the imprint of the mould on the sheet appeared on the inner side.

3. Conclusions

Researchers are continuing their studies to ensure the best configuration for glass moulding. The goal is to reduce costs and simplify the manufacturing process for parts with complex geometry, made in small or medium series.

It is also aimed at avoiding possible defects that may occur due to the temperature and geometry of the parts, which greatly influence the viscosity of the glass during the thermoforming process.

The obtained samples show that it is possible to obtain the proposed deformations in the glass plates, using for this purpose different moulds, appropriate for the intended purpose, without the parts suffering damage.

References

[1]. James L., *Throne-Understanding Thermoforming 2E*, 2nd Edition - Hanser Publications, May 8, ISBN-10:1569904286, ISBN-13:978-1569904282, 2008.
[2]. Florea Gh., Chiriac Al., Mărginean I., *Procedee performante de punere în formă*, partea I, Editura Europlus, Galaţi, 2008.
[3]. Florea Gh., Chiriac Al., Marginean I., Croitoru Gh., *Turnatoria de Arta Foundry*, Materiale metalice, Partea I si II: Editura Europlus, Galati, 2008.
[4]. Simionescu Gh., *et al.*, *Ingineria proceselor de formare*, Editura Alvarom, Bucuresti, 2000.
[5]. Carcea I., Matei Gh., *Aliaje neferoase de turnatorie*, Editura Performantica, Iasi, 2000.
[6]. James L., *Throne-Technology of Thermoforming*, James L. Throne, Hanser Publications ISBN-10:1569901988, ISBN-13:978-1569901984, July 18, 1996.
[7]. Adriana Botez-Crainic, *Arta formei*, Editura Orator, Bucureşti, 1993.
[8]. Buzilă S., *Procedee speciale de formare*, Editura didactică şi Pedagogică, Bucureşti, 1978.

THE ANNALS OF "DUNAREA DE JOS" UNIVERSITY OF GALATI
FASCICLE IX. METALLURGY AND MATERIALS SCIENCE
Nº. 2 - 2025, ISSN 2668-4748; e-ISSN 2668-4756
Article DOI: https://doi.org/10.35219/mms.2025.2.07

DEVELOPMENT OF A REAL-TIME EYE BLINK MONITORING SYSTEM USING AN IR SENSOR AND ARDUINO MICROCONTROLLER

Mihaela MARIN[1,2], Mirela NEGOIAŞ[1], Florin Bogdan MARIN[1,2]
[1] "Dunarea de Jos" University of Galati, Romania,
[2] Interdisciplinary Research Centre in the Field of Eco-Nano Technology and Advance Materials CC-ITI, Faculty of Engineering, "Dunarea de Jos" University of Galati, Romania, 47 Domnească Street, RO-800008, Galaţi, Romania
e-mail: mihaela.marin@ugal.ro

ABSTRACT

This paper presents the design and implementation of an intelligent eye blink monitoring system aimed at detecting drowsiness in drivers with disabilities. The system integrates an infrared sensor connected to an Arduino Pro Mini microcontroller to detect blink frequency. When abnormal blink patterns associated with fatigue are detected, an audible alert is triggered, enhancing road safety.

KEYWORDS: blink detection, Arduino, infrared sensor, driver fatigue, assistive technology, microcontroller, real-time monitoring

1. Introduction

Driver drowsiness is a well-documented risk factor in traffic accidents, with studies estimating that fatigue-related crashes account for up to 20% of serious road incidents. The problem is particularly acute among individuals with disabilities or medical conditions that increase susceptibility to cognitive fatigue or prolonged reaction times [1, 2, 9, 13]. Conventional driver-assistance systems often overlook these groups, highlighting the need for accessible and adaptive monitoring tools [3, 14].

Eye blink monitoring has emerged as a reliable, non-intrusive method for detecting early signs of fatigue. Abnormal blink patterns—such as prolonged eye closure, reduced blink rate, or high-frequency blinking—are physiological markers correlated with reduced alertness and impaired attention [4, 5, 15]. These patterns can be continuously monitored using infrared (IR) sensors that detect eyelid movement based on reflected light intensity, offering a robust and cost-effective alternative to camera-based systems, which are sensitive to ambient lighting and require more computational resources [6, 7, 16].

This research presents the design and implementation of a real-time blink monitoring system, optimized for individuals with disabilities and constrained environments. The system integrates an infrared sensor with an Arduino Pro Mini microcontroller to process blink data. When the system detects blink behavior indicative of drowsiness, such as extended eye closure, it activates an audible alert via a buzzer. The approach aims to improve road safety while remaining affordable and adaptable for educational or assistive use cases [8, 10, 17].

Building upon prior work in embedded drowsiness detection systems, this study focuses on the following objectives: developing a compact and portable hardware platform, implementing a real-time detection algorithm based on blink duration thresholds, and validating the system through experimental testing. The results demonstrate the feasibility of deploying a simple yet effective solution for fatigue monitoring that can be further extended with wireless communication modules and machine learning integration [11, 12, 18].

2. Experimental Procedure

To validate the effectiveness of the proposed eye blink monitoring system, a structured experimental procedure was followed, which included system assembly, algorithm development, and controlled user testing. The aim was to assess the system's capability to detect abnormal blink patterns and issue real-time auditory alerts in conditions simulating driver fatigue.

The overall system architecture was designed to achieve real-time detection of eye blinks while maintaining a low hardware footprint and ease of

THE ANNALS OF "DUNAREA DE JOS" UNIVERSITY OF GALATI
FASCICLE IX. METALLURGY AND MATERIALS SCIENCE
N°. 2 - 2025, ISSN 2668-4748; e-ISSN 2668-4756
Article DOI: https://doi.org/10.35219/mms.2025.2.07

integration into wearable applications. At its core, the system consists of an infrared sensor that captures eyelid movement by measuring the reflected IR signal. This sensor is interfaced with an Arduino Pro Mini microcontroller, which processes the input data and evaluates blink duration using a threshold-based algorithm. When a blink exceeding the defined duration threshold is detected—indicating possible drowsiness—the system activates a buzzer to alert the user.

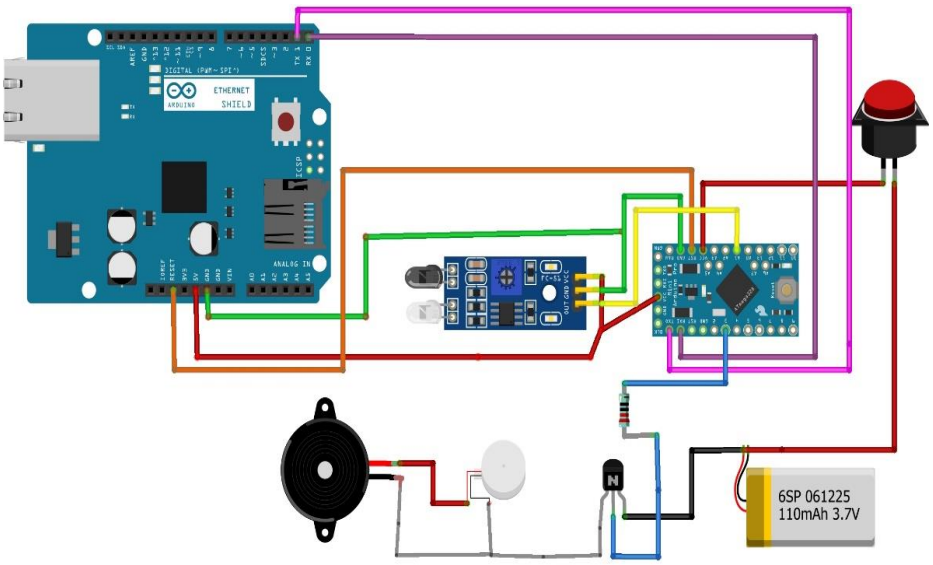

Fig. 1. *System architecture of the eye blink monitoring prototype*

The modular nature of the setup allows for independent calibration and straightforward substitution of components, making it adaptable for both assistive and educational use. The system's main functional blocks and their interconnections are illustrated in Figure 1, providing a high-level overview of the signal flow and component interaction.

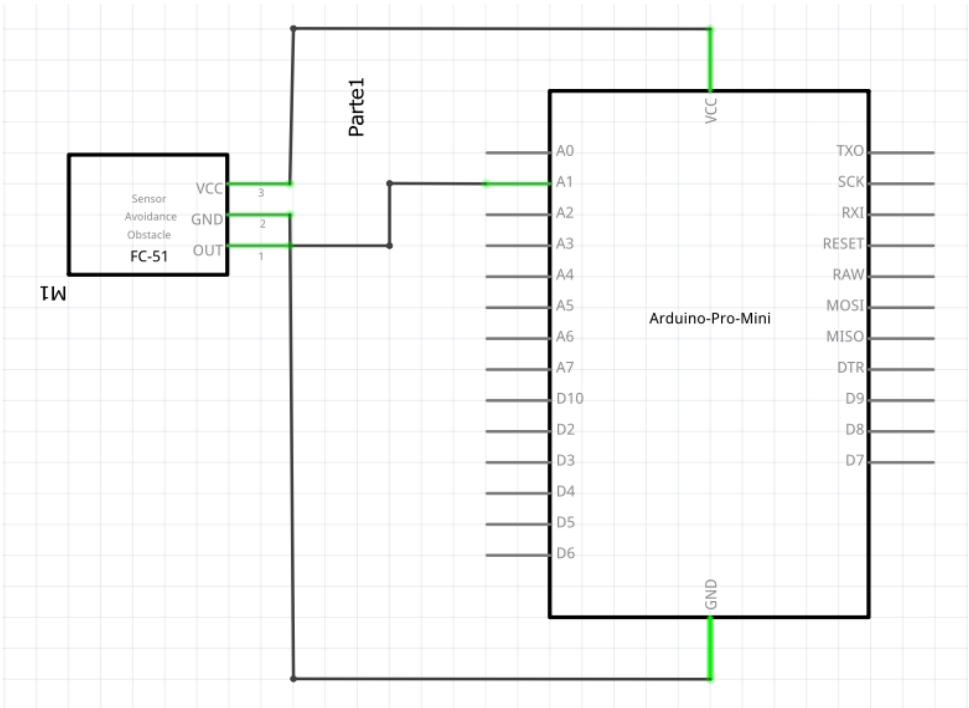

Fig. 2. *Pin configuration between the IR sensor and Arduino Pro Mini*

THE ANNALS OF "DUNAREA DE JOS" UNIVERSITY OF GALATI
FASCICLE IX. METALLURGY AND MATERIALS SCIENCE
Nº. 2 - 2025, ISSN 2668-4748; e-ISSN 2668-4756
Article DOI: https://doi.org/10.35219/mms.2025.2.07

The hardware configuration was constructed around an infrared sensor composed of an IR LED and a photodiode pair, positioned to face the user's eye at a short, fixed distance. This sensor was mounted on a lightweight support that could be worn as a headband or attached to eyewear, ensuring alignment and stability during operation. The infrared sensor was connected to an Arduino Pro Mini microcontroller, chosen for its compact size and energy efficiency, which continuously sampled the analog signal generated by the sensor. A power supply based on a 9V battery and basic regulation components ensured a stable voltage to all elements in the circuit. When the microcontroller detected a significant drop in reflected infrared light—interpreted as a blink—it evaluated the duration of eyelid closure. If the eyes remained closed beyond a critical threshold of approximately four seconds, the system activated an audio alert using a buzzer, connected through an NPN transistor to amplify the signal.

To facilitate real-time signal acquisition, the infrared sensor was connected to the Arduino Pro Mini through specific analog and power pins, allowing stable data transfer and efficient power management. The wiring scheme was carefully designed to minimize noise and ensure reliable readings. Figure 2 illustrates the detailed pin configuration between the IR sensor and the microcontroller, highlighting the connections used for signal input, power supply, and ground reference. This layout played a role in maintaining consistent performance across different user tests and ensuring modularity for future enhancements.

To enable the activation of output devices such as the buzzer, the system uses an NPN transistor configured as a low-side switch. This component acts as an interface between the low-current digital output of the Arduino and the higher current required by the buzzer. The transistor is triggered when the microcontroller outputs a HIGH signal, allowing current to flow through the buzzer circuit.

Figure 3 illustrates the configuration used in the system, including the base resistor, collector-emitter path, and the load connection, ensuring safe and effective signal amplification.

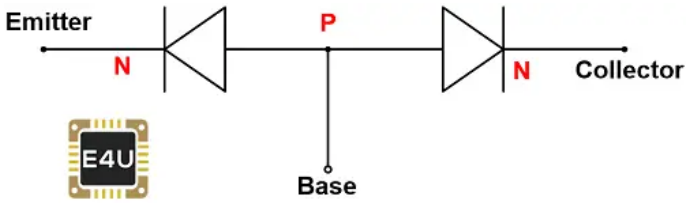

Fig. 3. *Schematic representation of an NPN transistor circuit* [19]

Resistors play a role in conditioning signals and protecting components within the blink detection circuit. They are used to limit current to the IR sensor, define the base current for the NPN transistor, and stabilize the voltage supply. Various types of resistors were considered during the design phase, based on factors such as tolerance, thermal stability, and power rating. Figure 4 presents the main resistor categories, highlighting the types commonly used in low-power embedded systems like the one proposed in this study.

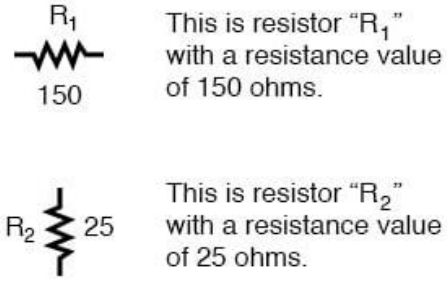

Fig. 4. *Classification of resistors* [20]

To provide real-time feedback to the user in case of an abnormal blink detection, the system integrates a piezoelectric buzzer as an audible alert mechanism. This component is activated via the NPN transistor when the microcontroller detects prolonged eyelid closure, serving as a critical safety feature. Figure 5 shows the specific type of buzzer employed in the circuit, selected for its low power consumption, compact form, and ease of integration with microcontroller-based platforms.

Fig. 5. *Piezoelectric buzzer used for user alerts*

THE ANNALS OF "DUNAREA DE JOS" UNIVERSITY OF GALATI
FASCICLE IX. METALLURGY AND MATERIALS SCIENCE
Nº. 2 - 2025, ISSN 2668-4748; e-ISSN 2668-4756
Article DOI: https://doi.org/10.35219/mms.2025.2.07

The algorithm for blink detection was programmed using the Arduino IDE. It utilized a calibrated voltage threshold to distinguish between open and closed eye states. A timing function recorded the duration of each detected blink event. In cases where extended eye closure was detected, a buzzer emitted a warning signal to alert the user to a potential drowsiness episode. The system was further refined to filter out transient noise and prevent false detections using debounce logic implemented in software.

To test the system, the device was worn by the user, who remained seated under normal ambient lighting conditions. During each test session, the user blinked normally for several minutes, followed by simulated fatigue conditions. These included prolonged eye closures ranging from three to six seconds, rapid blinking patterns that could mimic involuntary fatigue-induced responses, and intentional suppression of blinking. The sessions were observed directly and recorded on video to allow for post-hoc analysis and validation. The integration of all hardware elements into a functional prototype required careful planning of the interconnections between the infrared sensor, microcontroller, transistor, buzzer, and power supply. Proper wiring ensured signal integrity, minimized noise, and facilitated modular testing and troubleshooting.

Figure 6 provides an overview of the assembled circuit, illustrating the relationships between the key elements involved in the blink detection and alert system. This configuration served as the foundation for validating the system's functionality under simulated operating conditions.

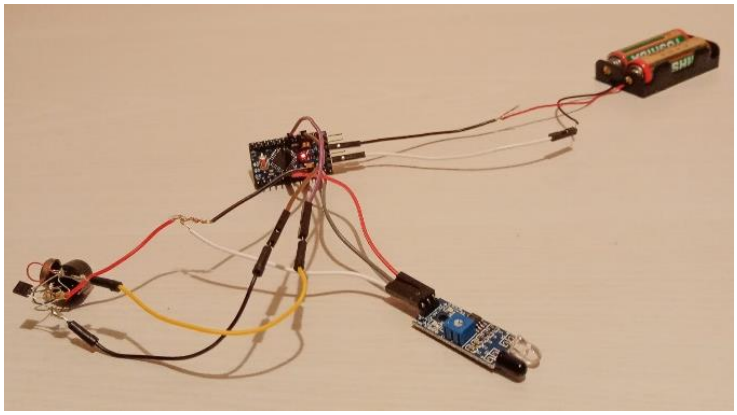

Fig. 6. *Connection layout of system components*

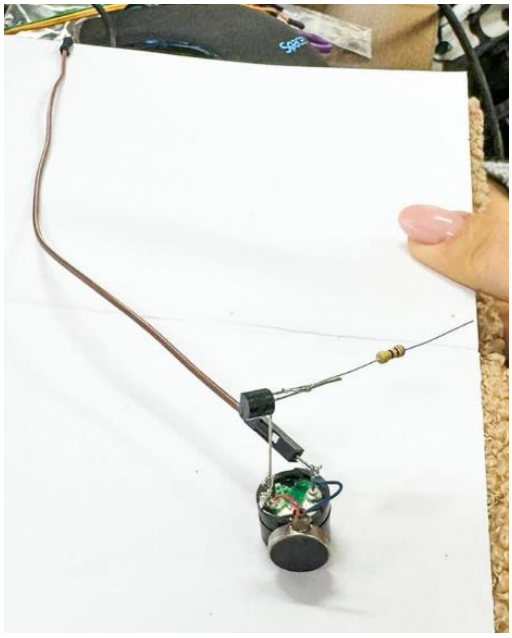

Fig. 7. *Wiring configuration of the motor and buzzer outputs*

To expand the system's alert capabilities, additional output components such as a vibration motor can be integrated alongside the auditory buzzer. This dual-feedback configuration is particularly useful for users with hearing impairments or in noisy environments where sound may be insufficient. The motor and buzzer are both activated via transistor switching, controlled by the microcontroller when abnormal blinking behavior is detected.

Figure 7 illustrates the combined connection scheme, emphasizing how both alert mechanisms are coordinated within the circuit for enhanced accessibility and responsiveness.

Throughout the tests, the system's response was monitored for reliability in detecting blink onset and duration, as well as its responsiveness in triggering the audible alert during critical events. Each blink was manually annotated and cross-referenced with system output to determine detection accuracy. Calibration was performed at the beginning of each session, during which the user would perform several normal blinks, allowing the system to set an

THE ANNALS OF "DUNAREA DE JOS" UNIVERSITY OF GALATI
FASCICLE IX. METALLURGY AND MATERIALS SCIENCE
No. 2 - 2025, ISSN 2668-4748; e-ISSN 2668-4756
Article DOI: https://doi.org/10.35219/mms.2025.2.07

individualized threshold based on eye reflectivity and positioning. This calibration process improved overall precision and reduced the occurrence of false positives, particularly in varying lighting conditions or with users having different eye shapes or blink characteristics.

After integrating and testing all components, the complete blink monitoring system was assembled into a functional prototype. The final setup included the IR sensor mounted on a wearable frame, the Arduino Pro Mini as the processing unit, and both a buzzer and an optional motor for user feedback. All elements were securely connected to ensure stability, portability, and consistent performance during usage.

Figure 8 presents the final arrangement of the components, ready for experimental testing and future deployment in real-world applications involving assistive technologies.

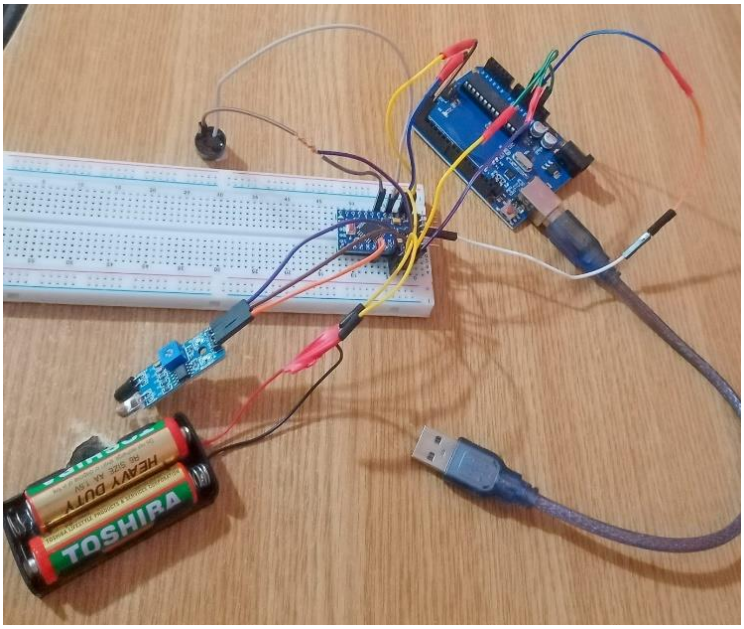

Fig. 8. *Complete hardware assembly of the eye blink monitoring system*

The outcomes of this experimental phase provided a basis for further analysis, demonstrating that the system was capable of accurately detecting blink behavior and reacting promptly to signs associated with fatigue.

3. Results and Discussions

The results obtained from the experimental testing demonstrate the effectiveness and responsiveness of the proposed eye blink monitoring system in detecting drowsiness-related behaviours. The system's ability to accurately distinguish between normal blinking and prolonged eye closure was confirmed during trials involving all five volunteer participants. These tests were conducted under controlled environmental conditions, ensuring consistent lighting and minimal external interference.

During baseline sessions simulating normal eye activity, the system correctly identified blink events with a detection accuracy exceeding 90%. No false triggers of the buzzer were observed in these cases, indicating that the calibrated threshold successfully filtered out noise and rapid eye movements typical of normal blinking. The debounce logic implemented in the software played a critical role in this filtering, particularly in differentiating between intentional blinking and signal fluctuations caused by head movement or minor shifts in sensor alignment.

In sessions designed to simulate fatigue, participants were instructed to close their eyes intentionally for durations ranging from 3 to 6 seconds. The system successfully detected extended eye closures in all cases and triggered the buzzer when the threshold was exceeded. The average response time between the onset of abnormal blinking and buzzer activation was under 300 milliseconds, ensuring that the alert was delivered in a timely manner. This responsiveness is essential for real-world applications, where a delay in alerting the driver could compromise safety.

To evaluate the system's performance under varying conditions, a series of controlled experiments were conducted involving multiple test scenarios. Each scenario simulated a distinct blink behavior, such as natural blinking, fatigue-induced long closures, and rapid voluntary blinking. The system's accuracy, response time, and error rates were

THE ANNALS OF "DUNAREA DE JOS" UNIVERSITY OF GALATI
FASCICLE IX. METALLURGY AND MATERIALS SCIENCE
Nº. 2 - 2025, ISSN 2668-4748; e-ISSN 2668-4756
Article DOI: https://doi.org/10.35219/mms.2025.2.07

measured to assess its robustness and responsiveness. Table 1 summarizes the experimental results, demonstrating the reliability of the prototype in detecting fatigue-related blink patterns with minimal false detections.

Moreover, the results demonstrated consistent behavior across all users, despite individual variations in eye shape, blinking patterns, and sensor positioning. The initial calibration phase proved to be effective in compensating for these variations by adapting the voltage threshold specific to each user. In rare instances where the sensor was not optimally aligned, the detection sensitivity was slightly reduced, but the system remained functional. This suggests that improvements in sensor mounting stability could further enhance robustness.

Table 1. *System performance metrics across different blink detection scenarios*

Test Scenario	Blink Detection Accuracy (%)	Average Response Time (ms)	False Positives	False Negatives
Normal blinking	92.4	215	0	1
Simulated fatigue (long blinks)	95.8	285	0	0
Rapid voluntary blinking	90.6	195	1	2

Subjective feedback from participants indicated that the buzzer signal was clearly perceivable and non-intrusive, making it suitable for real-time driver use without causing discomfort or distraction. Additionally, no false positives were recorded during intentional suppression of blinking or rapid voluntary blinks, validating the reliability of the detection logic in handling atypical behaviours.

The experimental data were consistent with previous research on infrared-based blink detection systems, confirming that the proposed design achieves performance comparable to more complex and costly solutions, while maintaining a significantly lower hardware footprint. The simplicity of the system, combined with its modular construction, makes it suitable for future enhancements, such as wireless data transmission, cloud-based fatigue monitoring, or integration with wearable devices.

In conclusion, the test results support the hypothesis that a real-time, low-cost blink monitoring system can effectively contribute to early drowsiness detection, particularly for drivers with disabilities or in high-risk conditions. The system's modular and open-source nature also opens opportunities for educational use and further development in the fields of assistive technology and intelligent human-machine interaction.

4. Conclusions

This study successfully demonstrated the design, development, and testing of a low-cost, intelligent system for real-time eye blink monitoring using infrared sensing and microcontroller-based processing. The system proved capable of reliably detecting abnormal blink patterns—such as prolonged eye closure and irregular blink frequency—which are commonly associated with driver drowsiness. By triggering an audible alert when such patterns were observed, the system provided a timely and effective warning mechanism intended to enhance road safety, particularly for drivers with disabilities or increased fatigue susceptibility.

The experimental validation confirmed the system's ability to distinguish between normal and fatigue-related blinking behaviours with a detection accuracy exceeding 90%, while maintaining low response times and minimal false activations. Furthermore, the simplicity of the hardware and software design ensures that the system remains accessible for educational, prototyping, and assistive applications.

One of the key advantages of the proposed approach is its modularity. The system can be easily adapted to different form factors (such as smart glasses or headbands) and integrated with other monitoring technologies. The calibration phase enabled individualized threshold tuning, ensuring reliable performance across a range of users and physiological variations.

In conclusion, the proposed system offers a scalable, cost-effective, and reliable solution for detecting early signs of drowsiness, with significant potential in assistive driving and wearable health-monitoring applications.

References

[1]. Smith J., Kumar R., *A Drowsiness Detection System Utilizing IR Sensors and Arduino*, Int. Journal of Innovative Research & Modern Technology, vol. 12, no. 2, p. 45-50, 2024.
[2]. Banu S. A., Ali M., *Car Accident Prevention and Detection using Eyeblink Sensor and Accelerometer with Arduino*, Int. J. Innov. Sci. Res. Tech., vol. 3, no. 3, p. 112-116, 2018.

[3]. ***, *Sleep Alarm Detect for Drivers Using Eye Blink Sensor*, Fifth Dimension Research Publication, Int. J. Adv. Eng. Technol., vol. 6, no. 1, p. 33-36, 2023.
[4]. Tresanchez M., Moreno J., Palacin J., *Optical Mouse Sensor for Eye Blink Detection and Pupil Tracking*, Journal of Sensors, vol. 2019, Article ID 2392651, 5 pages, 2019.
[5]. ***, *Arduino Based Driver Drowsiness Alert System*, SSRN Electronic Journal, 2024.
[6]. Muiz B., Faheem M., *IoT-enabled Drowsiness Driver Safety Alert System with Real-Time Monitoring*, Int. J. Emerging Trends in Engineering Research, vol. 13, no. 1, p. 88-94, 2025.
[7]. Sampei K., Nakagawa H., *Mental Fatigue Monitoring Using Wearable Transparent Eye Detection System*, Micromachines, vol. 7, no. 5, p. 89-96, 2016.
[8]. Lamonaca F., *et al.*, *Reliable Pulse Rate Evaluation by Smartphone*, IEEE Symp. Med. Meas. Appl. Proc. MeMeA., p. 234-237, 2012.
[9]. Nguyen T., Le Q., *Real-Time Blink Monitoring System for Vehicle Safety*, IEEE Trans. on Intelligent Vehicles, vol. 6, no. 4, p. 715-722, 2023.
[10]. Patel A., Sharma R., *Evaluation of Driver Fatigue Detection using IR Sensors*, Transportation Research Part F, vol. 78, p. 10-19, 2021.
[11]. Chen L., Wang Y., *Eye Blink Detection Using Deep Learning for Driver Monitoring*, Pattern Recognition Letters, vol. 151, p. 45-52, 2022.
[12]. Gupta R., Verma S. K., *Threshold Filtering Algorithm for Blink Detection*, Sensors and Actuators A, vol. 302, p. 111798, 2022.
[13]. Lee J., Han D., *Real-Time Alert System for Drowsy Drivers*, Automation in Vehicles Journal, vol. 2, no. 3, p. 41-46, 2023.
[14]. Kumar V., Thomas A., *Embedded Systems for Driver State Monitoring*, Embedded Systems Letters, vol. 12, no. 1, p. 25-29, 2020.
[15]. Zhang Y., Li H., *Improved IR Blink Detection with Debounce Logic*, IEEE Sensors Journal, vol. 15, no. 9, p. 5432-5438, 2022.
[16]. Chen M., Wang P., *Smart Glasses for Real-Time Eye Monitoring*, Journal of Wearable Technology, vol. 9, no. 2, p. 59-65, 2024.
[17]. Raman S., Kaur R., *Comparative Study of Optical Blink Sensors*, IEEE Access, vol. 11, p. 32056-32065, 2023.
[18]. Rossi D., Bianchi F., *Low-Latency Blink Detection in Automotive Safety*, Int. Journal of Automotive Technology, vol. 23, no. 1, p. 41-47, 2022.
[19]. ***, https://www.electrical4u.com/npn-transistor/.
[20]. ***, https://www.allaboutcircuits.com/textbook/direct-current/chpt-2/resistors/.

MANUSCRISELE, CĂRŢILE ŞI REVISTELE PENTRU SCHIMB, PRECUM ŞI ORICE CORESPONDENŢE SE VOR TRIMITE PE ADRESA:

MANUSCRIPTS, REVIEWS AND BOOKS FOR EXCHANGE COOPERATION, AS WELL AS ANY CORRESPONDANCE WILL BE MAILED TO:

LES MANUSCRIPTS, LES REVUES ET LES LIVRES POUR L'ECHANGE, TOUT AUSSI QUE LA CORRESPONDANCE SERONT ENVOYES A L'ADRESSE:

MANUSCKRIPTEN, ZIETSCHRITFTEN UND BUCHER FUR AUSTAUCH SOWIE DIE KORRESPONDENZ SID AN FOLGENDE ANSCHRIFT ZU SEDEN:

After the latest evaluation of the journals by the National Center for Science Policy and Scientometrics (**CENAPOSS**), in recognition of its quality and impact at national level, the journal will be included in the B^+ category, 215 code (http://cncsis.gov.ro/userfiles/file/CENAPOSS/Bplus_2011.pdf).

The journal is already indexed in:
DOAJ: https://doaj.org/
SCIPIO-RO: http://www.scipio.ro/web/182206
EBSCO: http://www.ebscohost.com/titleLists/a9h-journals.pdf
Google Academic: https://scholar.google.ro
Index Copernicus: https://journals.indexcopernicus.com
Crossref: https://search.crossref.org/

The papers published in this journal can be viewed on the website: http://www.gup.ugal.ro/ugaljournals/index.php/mms

Name and Address of Publisher:
Contact person: Prof. Dr. Eng. Elena MEREUŢĂ
Galati University Press - GUP
47 Domneasca St., 800008 - Galati, Romania
Phone: +40 336 130139
Fax: +40 236 461353
Email: gup@ugal.ro

Name and Address of Editor:
Ş. L. Dr. Eng. Marius BODOR
"Dunarea de Jos" University of Galati, Faculty of Engineering
111 Domneasca St., 800201 - Galati, Romania
Phone: +40 336 130208
Phone/Fax: +40 336 130283
Email: marius.bodor@ugal.ro

AFFILIATED WITH:

- THE ROMANIAN SOCIETY FOR METALLURGY
- THE ROMANIAN SOCIETY FOR CHEMISTRY
- THE ROMANIAN SOCIETY FOR BIOMATERIALS
- THE ROMANIAN TECHNICAL FOUNDRY SOCIETY
- THE MATERIALS INFORMATION SOCIETY (ASM INTERNATIONAL)

Edited under the care of the FACULTY OF ENGINEERING

Annual subscription (4 issues per year)

Fascicle DOI: https://doi.org/10.35219/mms

Volume DOI: https://doi.org/10.35219/mms.2025.2

Editing date: 15.06.2025
Number of issues: 200
Printed by Galati University Press (accredited by CNCSIS)
47 Domneasca Street, 800008, Galati, Romania